bioRxiv preprint doi: https://doi.org/10.1101/624700; this version posted May 2, 2019. The copyright holder for this preprint (which was not certified by peer review) is the author/funder. All rights reserved. No reuse allowed without permission.

In vivo functional diversity of midbrain dopamine neurons within identified axonal projections

Navid Farassat[1], Kauê M. Costa [1a], Stefan Albert[2], Lora Kovacheva[1],
Josef Shin[1], Mahalakshmi Somayaji[1b], Gaby Schneider[2],
Jochen Roeper[1*]

Institute for Neurophysiology[1] and Institute for Mathematics[2]
Goethe University Frankfurt, Germany

[a] present address: National Institute on Drug Abuse Intramural Research Program, National Institutes of Health, Baltimore, USA

[b] present address: Department of Psychiatry, Columbia University, New York, USA

* Contact Info:

Prof. Dr. Jochen Roeper

Institute for Neurophysiology

Neuroscience Center, Goethe University

Theodor-Stern-Kai 7, 60590 Frankfurt, Germany

e-mail: roeper@em.uni-frankfurt.de

Tel: +49-69-6301-84091/92

bioRxiv preprint doi: https://doi.org/10.1101/624700; this version posted May 2, 2019. The copyright holder for this preprint (which was not certified by peer review) is the author/funder. All rights reserved. No reuse allowed without permission.

Abstract

The functional diversity of midbrain dopamine (DA) neurons ranges across multiple scales, from differences in intrinsic properties and synaptic connectivity to selective task engagement in behaving animals. Distinct *in vitro* biophysical features of DA neurons have been associated with different axonal projection targets. However, it is unknown how this translates to different firing patterns of projection-defined DA subpopulations in the intact brain. We combined retrograde tracing with single-unit recording and juxtacellular labelling in mouse brain to create the first single cell-resolved *in vivo* functional topography of the midbrain DA system. We identified surprising differences in burst firing among those DA neurons projecting to dorsolateral striatum, which were organized along the medio-lateral substantia nigra (SN) axis. Furthermore, burst properties also differentiated DA neurons in the medial SN that projected either to dorsal or ventral striatum. In contrast, DA neurons projecting to lateral shell of nucleus accumbens displayed identical firing properties, irrespective of whether they were located in the SN or ventral tegmental area (VTA), thus breaching classical anatomical boundaries. Finally, we found robust differences in mean firing rates and pause durations among VTA DA neurons projecting to either lateral or medial shell of nucleus accumbens. Together, our data set establishes a high-resolution functional landscape of midbrain DA neurons, which will facilitate the identification of selective functions and pathophysiological changes within the midbrain DA system.

Keywords dopamine, retrograde tracing, single-unit recording, substantia nigra, ventral tegmental area

bioRxiv preprint doi: https://doi.org/10.1101/624700; this version posted May 2, 2019. The copyright holder for this preprint (which was not certified by peer review) is the author/funder. All rights reserved. No reuse allowed without permission.

Introduction

The functional properties and the emerging diversity of the midbrain dopamine (DA) system have been extensively studied across many different biological scales (Schultz, 2015; Watabe-Uchida et al., 2017). These differences range from the single-cell level, including diverging gene expression profiles (Kramer et al., 2018; Nichterwitz et al., 2016; Poulin et al., 2018; Saunders et al., 2018a; Tiklova et al., 2019), cellular and biophysical properties (Evans et al., 2017; Lammel et al., 2008; Tarfa et al., 2017), as well as neurotransmitter co-release (Chuhma et al., 2018; Kim et al., 2015b; Tritsch et al., 2012; Zhang et al., 2015), up to different neural circuit affiliations (Beier et al., 2019; Beier et al., 2015; Lammel et al., 2012; Lerner et al., 2015; Menegas et al., 2015; Ogawa et al., 2014; Tian et al., 2016; Watabe-Uchida et al., 2012) and selective task engagement of DA subpopulations in awake behaving rodents (Dautan et al., 2016; de Jong et al., 2019; Duvarci et al., 2018; Gunaydin et al., 2014; Howe and Dombeck, 2016; Keiflin et al., 2019; Lammel et al., 2012; Matthews et al., 2016; Menegas et al., 2018; Menegas et al., 2017; Parker et al., 2016; Patriarchi et al., 2018; Saunders et al., 2018b; Vander Weele et al., 2018; Yang et al., 2018) and non-human primates (Kim et al., 2015a; Matsumoto and Hikosaka, 2009; Matsumoto and Takada, 2013; Ogasawara et al., 2018). Moreover, additional methods complementing classical single unit recordings, including voltammetric and fluorometric measurements of DA release (Dreyer et al., 2016; Hamid et al., 2016; Howe et al., 2013; Kishida et al., 2016; Lippert et al., 2019; Patriarchi et al., 2018) and *in vivo* calcium imaging of DA axons in distinct striatal areas (Howe and Dombeck, 2016) further support the notion of a multi-layered diversity of the DA system *at work* (Berke, 2018).

bioRxiv preprint doi: https://doi.org/10.1101/624700; this version posted May 2, 2019. The copyright holder for this preprint (which was not certified by peer review) is the author/funder. All rights reserved. No reuse allowed without permission.

Rather than a single global computation, the midbrain DA system has therefore emerged as a parallel processor carrying out multiple functions (Haber, 2014; Kegeles et al., 2010). Support for the concept that different DA neuron subtypes carry out different computational processes arose from the mapping of their *in vitro* cellular properties in combination with retrograde tracing. This showed that projection-identified groups of DA neurons, including those that project to specific subregions of the striatum, have marked differences in intrinsic biophysical properties and input-output relationships (Lammel et al, 2008; Tarfa et al 2017).

Distinct DA subpopulations are also differentially affected by pathological processes driving major brain disorders such as Parkinson disease (PD) (Obeso et al., 2017), schizophrenia (McCutcheon et al., 2019) or drug abuse (Luscher, 2016). In PD, a ventrolateral SN DA population is most severely affected (Damier et al., 1999; Fu et al., 2016; Gibb and Lees, 1991; Kordower et al., 2013), which might be indicative for an innate and/or acquired differential vulnerability towards alpha-synuclein aggregation-mediated neurodegeneration (Surmeier et al., 2017). In schizophrenia, PET-studies in patients strongly suggested an early and selective dysregulation of a DA subpopulation projecting to associative, dorsomedial striatal regions (Kegeles et al., 2010; McCutcheon et al., 2019), but cellular substrates have remained elusive. In models of drug addiction, a hierarchical sequence of DA release in different striatal territories has been identified (Willuhn et al., 2012). In depression models, based on chronic social defeat, selective hyperactivity in mesolimbic-projecting DA subpopulations has been identified as a causal factor in depression-like behaviors using projection-selective optogenetic interventions (Cao et al., 2010; Chaudhury et al., 2013; Tye et al., 2013).

bioRxiv preprint doi: https://doi.org/10.1101/624700; this version posted May 2, 2019. The copyright holder for this preprint (which was not certified by peer review) is the author/funder. All rights reserved. No reuse allowed without permission.

Therefore, there is increasing evidence that the classic triadic decomposition of the midbrain DA system (Bjorklund and Dunnett, 2007) into a dorsal mesostriatal, ventral mesolimbic, and cortical prefrontal arm might not be sufficiently granular to capture the functional and pathophysiological diversity of DA neurons. For example, the characteristic high-frequency "burst" discharge of midbrain DA neurons *in vivo* is most commonly associated with positive reward prediction error signaling (Schultz, 2015)(Cohen et al., 2012; Eshel et al., 2015) (Stauffer et al., 2016; Steinberg et al., 2013), but there is increasing evidence that – depending on the DA subtype – burst discharge plays also a role in other functions, including action control (da Silva et al., 2018; Jin and Costa, 2010) and the signaling of salience, novelty, anticipated fear or non-reward prediction errors, even in cells located in the same anatomical region (Kim et al., 2015a; Matsumoto and Hikosaka, 2009; Menegas et al., 2018; Schiemann et al., 2012). Nevertheless, the rapidly progressing dissection of DA controlled neuronal circuits using optogenetic and molecular tracing methods suggests this diversity in behavioral functions is matched to specific anatomical substrates (Beier et al., 2019; Beier et al., 2015; Lammel et al., 2012; Lerner et al., 2015; Menegas et al., 2015; Ogawa et al., 2014; Tian et al., 2016; Watabe-Uchida et al., 2012).

In order to help closing the current resolution gap between anatomy and physiology, it is therefore crucial to study the functional properties of DA neurons with identified axonal projections in the intact brain to better understand how intrinsic cellular differences and network affiliations jointly compute functional output. Accordingly, we carried out a systematic comparison of baseline *in vivo* electrical properties of anatomically and immunohistochemically verified midbrain DA neurons with identified axonal projections. Given our previous finding that even the innocuous labelling of DA neurons with GFP can affect their *in vivo* properties (Schiemann et al., 2012), we

bioRxiv preprint doi: https://doi.org/10.1101/624700; this version posted May 2, 2019. The copyright holder for this preprint (which was not certified by peer review) is the author/funder. All rights reserved. No reuse allowed without permission.

also aimed to carefully establish and control an experimental protocol for retrograde tracing that enabled us to register genuine differences of *in vivo* activity among DA neurons.

With this approach, we found a number of surprising results. First, we identified an unanticipated functional diversity among SN DA neurons, even among those sharing the same projections, targeting the dorsolateral striatum. However, this diversity followed a clear medial-to-lateral topography. Moreover, DA neurons with distinct axonal projections but overlapping distributions in the midbrain displayed different electrical properties regarding bursting, pausing, and even baseline mean frequencies. Only some of these identified *in vivo* differences were predicted based on previous studies of diverging intrinsic *in vitro* properties between distinct DA subpopulations (e.g. rebound delays and pausing) (Evans et al., 2017; Lammel et al., 2008; Tarfa et al., 2017), while other features, like differences in mean firing rates were surprising and indicated that certain neuronal network properties might override intrinsic differences in excitability. Overall, our study provides a refined functional *in vivo* landscape of the midbrain DA system embedded in an anatomical context of identified axonal projections.

bioRxiv preprint doi: https://doi.org/10.1101/624700; this version posted May 2, 2019. The copyright holder for this preprint (which was not certified by peer review) is the author/funder. All rights reserved. No reuse allowed without permission.

Results

Retrograde tracing with highly-diluted (0.002%) fluorogold preserves the natural *in vivo* electrophysiological properties of nigrostriatal dopamine neurons

Our aim was to characterize the electrophysiological *in vivo* properties of midbrain DA neurons with defined axonal projections in adult male C57Bl/6N mice. We noticed that the application of a conventional retrograde tracing protocol (2% fluorogold (FG); 500nl; 50nl/min; Liu et al. 2003) in the dorsal striatum (DS; bregma: 0.86 mm, lateral: 2.0 mm, ventral: 2.8 mm) resulted in structural damage of nigrostriatal axons already one week after infusion (Fig. 1A, column one, FG-0, note reduced TH expression). In contrast, we observed no apparent structural damage using a ten-fold FG-dilution (0.2%, Fig. 1A, FG-1, 2nd column from left), but surprisingly failed to detect any stable *in vivo* spontaneously active DA neurons in the substantia nigra (SN), again one week after infusion (N=3; ~10 tracts per animal, intra-nigral speed of electrode advancement 60µm/min; coverage 4-5mm Z-depth from skull, data not shown). However, in control animals using the same number of tracts and electrode parameters, we routinely detected between 3-6 SN DA neurons per animal (N=14, data not shown).

Thus, we carried out a systematic dilution series to define a working concentration of FG which would still result in substantial coverage of retrogradely labelled nigrostriatal DA neurons but at the same time maintain their stable *in vivo* electrophysiological properties, similar to those observed in control animals. With this strategy, we identified 0.002% FG (FG-3) to be the lowest concentration where a

bioRxiv preprint doi: https://doi.org/10.1101/624700; this version posted May 2, 2019. The copyright holder for this preprint (which was not certified by peer review) is the author/funder. All rights reserved. No reuse allowed without permission.

significant proportion (ca. 20-30%) of SN DA neurons displayed detectable tracer levels based on intrinsic FG fluorescence (Fig. 1A, FG-3, column four; Supplemental Fig. 1-1A, signal to noise 3:1). This rate of detection was further improved by using a FG-antibody (see M&M) combined with a fluorescently-labelled 2nd antibody (Figure 1B). The FG-antibody generated very low background in the ventral midbrain (contralateral side) resulting in an improved signal-to-noise ratio (see Supplemental Fig. 1-1A; Signal to noise 10:1). Detailed inspection of the cellular distribution of FG-immunoreactivity within DA neurons revealed selective immunostaining in cytoplasmic vesicles, most likely to be lysosomes (Wessendorf, 1991).

Next, we probed for the *in vivo* electrophysiological properties of FG-3 retrogradely labelled nigrostriatal DA neurons, one week after infusion, in comparison to those from control animals (Figure 2). All *in vivo* recorded neurons reported in this study were juxtacellularly labelled with neurobiotin to define their neurochemical nature (i.e. tyrosine hydroxylase (TH)-immunopositive = dopaminergic) and cellular position in the midbrain with the identification of their respective axonal projection targets, indicated by the FG signal in the labelled neuron. For a sensitive comparison between FG-3-labelled and control DA neurons, we focused on those in the lateral substantia nigra (lSN), given that they are the most vulnerable to cellular damage among midbrain DA neurons (Surmeier et al., 2017). Figure 2 compares the spontaneous *in vivo* activity of a DA-lSN neuron in a control animal (panels B1-B4) with one from a FG-3-labelled DA-lSN neuron of a traced mouse (panels C1-C4). Panel C4 displays the neurobiotin and FG-signal demonstrating that this DA-lSN neuron projected to the dorsolateral striatum (DLS; bregma: 0.86 mm, lateral: 2.2 mm, ventral: 2.6 mm) and - similarly to the control neuron (panel B4) - was located in the lSN at bregma -3.08mm. Note that discharge frequencies and patterns as well as

bioRxiv preprint doi: https://doi.org/10.1101/624700; this version posted May 2, 2019. The copyright holder for this preprint (which was not certified by peer review) is the author/funder. All rights reserved. No reuse allowed without permission.

the single action potential waveforms are very similar between the control (panel B1-B3) and the FG-3-labelled DA neuron (panel C1-C3).

Figure 3 summarizes the electrophysiological group data of retrogradely labelled DA-lSN neurons compared to DA controls in the same regions. The completely overlapping cellular positions of these two groups are depicted in Figure 3A. The inset shows the representative FG-injection site in the DLS. In line with the examples shown in Figure 2, quantitative analysis of firing frequency (means ± SEMs; control: 3.51 ± 0.41 Hz, FG: 3.51 ± 0.4 Hz; panel 3B), regularity (CV; control: 62.92 ± 7.55 %, FG: 58.84 ± 7.29 %; panel 3B) and quantitative descriptors of ISI-distribution patterns (kurtosis (control: 4.1 ± 0.73, FG: 3.69 ± 0.69), skewness (control: 0.98 ± 0.18, FG: 0.88 ± 0.16) and a firing pattern categorization based on a theoretical model called GLO (see methods), panel 3B) did not reveal any significant differences between the two populations. In addition, AP waveforms (AP duration (control: 2.04 ± 0.06 ms, FG: 1.94 ± 0.08 ms), relative AP trough (control: -0.63 ± 0.02, FG: -0.55 ± 0.04); panel 3C) and burst and pause properties were also unaffected (SFB (control: 11.93 ± 4.18 %, FG: 9.42 ± 3.57 %), SFB contingency (% of neurons > 5% SFB; control: 37.5 %, FG: 40 %), bursts per minute (control: 7.67 ± 2.8, FG: 6.28 ± 2.24), intraburst-frequency (control: 21.37 ± 5.74 Hz, FG: 18.94 ± 1.72 Hz); panels 3E and 3F; pauses per minute (control: 0.93 ± 0.88, FG: 2.05 ± 1.26), pause duration (control: 0.88 ± 0.25 s, FG: 0.7 ± 0.13 s); panel 3D; see Supplemental Fig. 3-1 for additional variables and their regional distributions). In summary, retrograde tracing with 1000-fold diluted FG did not perturb any *in vivo* electrophysiological property of lSN DA neurons. We assumed that less vulnerable DA populations residing in the medial SN and VTA are also likely to be unaffected by this FG labelling protocol. This

bioRxiv preprint doi: https://doi.org/10.1101/624700; this version posted May 2, 2019. The copyright holder for this preprint (which was not certified by peer review) is the author/funder. All rights reserved. No reuse allowed without permission.

in turn enabled us to compare authentic electrophysiological properties of DA midbrain subpopulations with defined axonal projections.

Dorsal and ventral striatal-projecting DA neurons intermix in the medial substantia nigra

Based on our previous work (Lammel et al., 2008) that demonstrated axonal-projection-related differences in *in vitro* electrophysiological properties of midbrain DA neurons, we selectively traced axonal target areas in the dorsolateral (DLS; bregma: 0.86 mm, lateral: 2.2 mm, ventral: 2.6 mm) and dorsomedial striatum (DMS; bregma: 0.74 mm, lateral: 1.4 mm, ventral: 2.6 mm) as well as in the lateral (lNAcc; bregma: 0.86 mm, lateral: 1.75 mm, ventral: 4.5 mm) and medial shell (mNAcc; bregma: 1.54 mm, lateral: 0.7 mm, ventral: 4.25 mm) of the nucleus accumbens (Figure 4A1-D1; n=3 animals each). One week after infusion, we mapped the cellular distributions of TH+ (i.e. dopaminergic) neurons characterized by these four different projections (Figure 4A2-D2). The overall topographic patterns of cellular distributions (see Supplemental Fig. 4-1) was in accordance with those from previous work using retrobeads (Lammel et al., 2008) or retrograde viral tracers (Lerner et al., 2015). We also combined the tracing with additional calbindin immunohistochemistry, which confirmed the well-known calbindin-TH coexpression pattern but did not help to differentiate between different axonal projections (Supplemental Fig. 4-2).

Our data revealed a high complexity within the medial SN, where DA cell bodies of three distinct, equally prevalent axonal projections intermingled (mSN; ~30% DLS, ~40% DMS, ~30% lNAcc). By contrast, in the two neighboring regions, the lSN and the lateral VTA (PBP/PN), only one axonal projection was dominant (~70% DLS-projecting DA neurons in the lSN; ~60% lNAcc in the PBP, ~70% mNAcc in the PN).

bioRxiv preprint doi: https://doi.org/10.1101/624700; this version posted May 2, 2019. The copyright holder for this preprint (which was not certified by peer review) is the author/funder. All rights reserved. No reuse allowed without permission.

These tracing results implied that just obtaining precise information on the cellular localization (SOURCE) of recorded DA neurons via juxtacellular labelling, in particular in the mSN, would be insufficient to capture the *in vivo* functional diversity of the DA system.

We then asked whether DA neurons from the same midbrain area (SOURCE) but with distinct axonal projections (TARGETS) displayed different *in vivo* electrophysiological properties (Fig. 4E2 – shared SOURCE & distinct TARGETS). We also compared DA neurons in the mSN with those in the lSN (SOURCES) that both projected to the same TARGET region, the dorsolateral striatum (Figure 4F2). Indeed, only the dorsolateral striatum, in contrast to dorsomedial and ventral striatum, received two equally prominent axonal projections from the mSN and the lSN (Figure 4F2).

Low *in vivo* burstiness in medial compared to lateral DLS-projecting SN DA neurons

We recorded, labelled and identified DLS-projecting DA neurons in the mSN as well as in the lSN. Figure 5 compares the electrophysiological properties of two DLS-projecting DA neurons localized in the lSN (Fig. 5A1-A4, C) and mSN (Fig. 5B1-B4, C), respectively. The original 10s sample recording traces, the 30s raster plots and the two ISI histograms indicate that the depicted DLS-lSN DA neuron discharged in a highly bursty pattern, which was completely absent in the regularly discharging DLS-mSN DA neuron. Importantly, while about 40% of DLS-projecting DA neurons in the lSN (n=6 of 15) displayed this type of robust bursting (SFB > 5%) throughout the

bioRxiv preprint doi: https://doi.org/10.1101/624700; this version posted May 2, 2019. The copyright holder for this preprint (which was not certified by peer review) is the author/funder. All rights reserved. No reuse allowed without permission.

recording period, none of the identified DLS-projecting DA neurons located in the mSN (n=0 of 9) fired in this bursty manner (Fig 5D). Comparison of the cumulative probability distributions of burstiness (percentage of spikes fired in bursts; SFB%) between the two DLS-projecting SN DA populations confirmed their differences in firing pattern. In contrast, detailed analysis of other electrophysiological parameters between the two DLS-projecting SN DA neurons detected no further differences (see Supplemental Fig. 5-1). We then identified the best subset of electrophysiological parameters in a linear discriminant analysis (LDA) using half of the data from the two DLS-projecting SN DA populations. Using the variables (burstiness (SFB), relative AP trough and precision of spiking ($\log(\sigma_2)$)), we could accurately classify the remaining DLS-projecting SN DA neurons into a lateral and medial group with a predictive power of 79.2% ($p<0.05$). When using the entire data set to train the linear classifier, almost all (92.6%) of DLS-projecting SN DA neurons were classified correctly (Fig. 5E). In summary, our data demonstrated that SN DA neurons projecting to the DLS possess distinct bursting properties *in vivo* depending on where they are located within the SN. We therefore identified a topographically organized (i.e. medial vs lateral) *in vivo* diversity among SN DA neurons sharing the same axonal projections to dorsolateral striatum.

Functional segregation of *in vivo* electrophysiological properties along distinct axonal projections of DA neurons in the medial substantia nigra

As described above (Fig. 4), retrograde tracing revealed that the mSN harbors equal proportions of DA neurons projecting to dorsolateral, dorsomedial or ventral striatum (i.e. lateral shell of nucleus accumbens). We asked whether DA mSN neurons with

bioRxiv preprint doi: https://doi.org/10.1101/624700; this version posted May 2, 2019. The copyright holder for this preprint (which was not certified by peer review) is the author/funder. All rights reserved. No reuse allowed without permission.

distinct axonal projections also display systematic functional differences *in vivo*. We first compared the *in vivo* electrophysiology of mSN DA neurons projecting to DLS (n=9, see Fig 5) with those projecting to DMS (n=9). Here, we found no differences between any parameters of these two mSN DA populations projecting to different territories of the dorsal striatum (see Supplemental Fig. 6-1). Accordingly, the linear discriminant analysis (LDA) based on the best set of parameters (CV, SFB, skewness of the ISI-distribution, pauses per minute, the mean oscillation period (GLO) and the relative AP trough) did not perform above chance (50.9%) in discriminating DLS- from DMS-projecting DA neurons in the medial SN. We conclude that DA neurons localized in the medial SN (SOURCE) and projecting to different dorsal striatal areas (DMS/DLS, TARGETS) did not show significant differences in their *in vivo* electrophysiological baseline properties. Consequently, they were pooled (DS) for functional comparison with ventral projecting mSN DA neurons.

Figure 6 compares the electrophysiological properties of two DA neurons in the mSN, projecting either to dorsal striatum (DS) or ventral striatum (i.e. lateral shell of nucleus accumbens, lNAcc). The 10s recording traces, 30s raster plots and the two ISI histograms show obvious functional differences (panels 6A and 6B). Apart from mean frequencies and AP waveforms, which were similar, most electrophysiological parameters describing the patterns of discharge including bursts (Figure 6D) but also pauses (Figure 6E), as well as the shapes of the ISI-distributions (Kurtosis, Skewness; Figure 6F) were significantly different between dorsal (n=18) and ventral (n=14) striatum projecting mSN DA neurons (Supplemental Fig. 6-2). The linear discriminant analysis (LDA) based on the best set of parameters (skewness of the ISI-distribution, AP duration, relative AP trough and the precision of spiking (log(σ2)) showed a strong trend to classify mSN DA neurons into dorsal or ventral striatum

bioRxiv preprint doi: https://doi.org/10.1101/624700; this version posted May 2, 2019. The copyright holder for this preprint (which was not certified by peer review) is the author/funder. All rights reserved. No reuse allowed without permission.

projecting cells with a predictive power of 70.8%, when using half of the data set for training ($p<0.07$). When the entire data set was used, 84.4% of mSN DA neurons were classified correctly (Fig. 6G). Furthermore, a functional comparison of lateral shell NAcc-projecting (TARGET) DA neurons localized in the mSN compared to those positioned in the VTA (SOURCES), the classical location of mesolimbic DA neurons, revealed no significant differences (see Supplemental Fig. 6-3) between the groups, violating the VTA/SN anatomical boundary. Therefore, lateral shell NAcc-projecting DA neurons from both mSN and VTA were pooled in further comparisons.

DA neurons projecting to medial or lateral shell of the nucleus accumbens display distinct *in vivo* mean firing rates

We next asked whether distinct ventral striatal-projecting populations (i.e. lateral shell NAcc vs medial shell NAcc-projecting neurons) also show functional differences *in vivo*, given that these two populations displayed very distinct electrophysiological properties *in vitro* (Lammel et al., 2008). Figure 7 compares the electrophysiological properties of two DA neurons in the VTA, projecting either to lateral shell (lNAcc) or medial shell (mNAcc) of nucleus accumbens. The 10s recording traces, 30s raster plots and the two ISI histograms display selective differences in mean discharge frequency and the duration of pauses only (Fig. 7A and 7B), which are also evident at the population level (Fig. 7D). In contrast, all other functional *in vivo* properties – including analyzed AP waveform parameters - did not differ between the two populations (see Supplemental Fig. 7-1). In light of the previous *in vitro* data, where medial shell NAcc-projecting DA neurons showed higher firing rates compared to lateral shell NAcc DA neurons, our *in vivo* results are surprising. In contrast, the

bioRxiv preprint doi: https://doi.org/10.1101/624700; this version posted May 2, 2019. The copyright holder for this preprint (which was not certified by peer review) is the author/funder. All rights reserved. No reuse allowed without permission.

longer *in vivo* pauses observed in medial shell NAcc projecting VTA DA neurons are in line with their very long *in vitro* post-inhibition rebound delays. Note that none of the subsets of variables used for linear discriminant analysis showed a segregation of these two mesolimbic DA populations above chance level.

Finally, we attempted to apply our approach to DA neurons projecting to medial prefrontal cortex (mPFC). While we succeeded in labelling and anatomically mapping this sparse DA subpopulation with our FG-3-protocoll, the success rate of identifying and labelling spontaneously active mPFC-projecting DA neurons was not sufficient (ca. 10%) to carry out a systematic study (Supplemental Fig. 7-2; 1 of 10 recorded and labelled VTA neurons was identified to be dopaminergic and projecting to mPFC). As our method depends on spontaneous *in vivo* activity, prefrontal-projecting DA neuron might have to be targeted in awake animals.

bioRxiv preprint doi: https://doi.org/10.1101/624700; this version posted May 2, 2019. The copyright holder for this preprint (which was not certified by peer review) is the author/funder. All rights reserved. No reuse allowed without permission.

Discussion

Our study refines the functional *in vivo* topography of midbrain DA neurons in several ways. We provide the first detailed description and anatomical mapping of axon projection-specific functional DA phenotypes *in vivo*. Importantly, all n=102 DA neurons in this study were labelled and immunohistochemically identified, thus avoiding the uncertainties of “putative” DA populations. Moreover, our study controlled for functional perturbations by retrograde labelling itself, based on our high-dilution fluorogold protocol. In comparison to our previous work characterizing the *in vitro* properties of DA neurons with distinct axonal projections (Lammel et al., 2008), we found a number of unexpected results *in vivo*. We did not anticipate the large degree of functional diversity regarding burst firing among those SN DA neurons projecting to dorsolateral striatum. Furthermore, we were surprised to find *in vivo* bursting of DA neurons in the medial SN to be exclusively associated with cells projecting to lateral shell of nucleus accumbens. Finally, the difference in mean firing rates between slower-discharging DA neurons projecting to medial shell and faster-firing DA neurons projecting to lateral shell of nucleus accumbens was unexpected given their respective intrinsic excitabilities. Overall, our findings provide an improved functional definition of distinct DA circuits operating in the intact brain.

Our study has a number of limitations. Importantly, all *in vivo* electrophysiological data were recorded under isoflurane anesthesia. Therefore, we cannot directly draw conclusions about behaviorally relevant activity patterns in DA subpopulations but rather identify differences in *in vivo* baseline excitability. We have previously shown that some of these differences are associated with altered behavior, as in the case of

bioRxiv preprint doi: https://doi.org/10.1101/624700; this version posted May 2, 2019. The copyright holder for this preprint (which was not certified by peer review) is the author/funder. All rights reserved. No reuse allowed without permission.

burst firing in the medial SN and novelty-induced locomotion (Schiemann et al., 2012). In addition, we also showed that differences in *in vivo* firing rates between VTA DA neurons identified under isoflurance anesthesia in a mouse model of cognitive impairment (Krabbe et al., 2015), were recapitulated in awake behaving animals (Duvarci et al., 2018). However, the task-related differences in firing were only revealed in awake behaving animals (Duvarci et al., 2018). A second limitation is that we tried but did not succeed in getting more than an anecdotal data set of medial prefrontal projecting DA neurons. The unique mismatch between the extent of retrograde labelling and the difficulty of identifying and recording mesocortical DA neurons *in vivo* indicated that this DA subpopulation might either be particularly vulnerable to our labelling protocol or mostly silent under isoflurane anesthesia. The latter possibility is not unlikely given the evidence for orexinergic modulation of mesocortical DA neurons (Del Cid-Pellitero and Garzon, 2014). Furthermore, our study focused on rostral striatal areas not covering the caudal “tail” region, which is a projection area of DA neurons located in the SN pars lateralis. This DA projection has been shown to be involved in the computing of aversive stimuli and stable visual memories in rodents and non-human primates (Kim et al., 2017; Kim et al., 2015a; Matsumoto and Hikosaka, 2009; Menegas et al., 2018; Menegas et al., 2015).

Our study has also a number of specific implications for future work. Given that labelling of DA subpopulations – for identification and/or optogenetic manipulation – has become an essential tool, we believe it is crucial to control whether the labelling itself will change functional properties of the target neurons *in vivo*. In addition to the effect of conventional concentrations of fluorogold, we have previously shown that virally-mediated GFP-expression in SN DA neurons leads to robust changes in their intrinsic firing pattern (Schiemann et al., 2012). We currently do not know how

bioRxiv preprint doi: https://doi.org/10.1101/624700; this version posted May 2, 2019. The copyright holder for this preprint (which was not certified by peer review) is the author/funder. All rights reserved. No reuse allowed without permission.

general – regarding the type of the label, the concentrations used and the timing post-injection - these perturbations of *in vivo* activity of DA neurons are.

Another notable result of our study is the large difference in burstiness between dorsolateral striatum projecting DA neurons in the medial compared to the lateral SN. While the underlying mechanisms need to be resolved, our findings are in line with a previous study from the Khaliq lab that found differences in *in vitro* excitability, including T-type calcium channel mediated rebound excitability, between calbindin-positive and calbindin-negative SN DA neurons (Evans et al., 2017). Also, Lerner and colleagues demonstrated larger HCN-currents in DLS-projecting SN DA neurons compared to DMS-projecting SN DA neurons, which might further enhance rebound excitability and possibly *in vivo* bursting (Lerner et al., 2015). In addition to the functional implications for nigrostriatal signaling, the enhanced burst excitability might also be of pathophysiological relevance. An influential hypothesis regarding the differential vulnerability between distinct DA subpopulations in Parkinson disease proposes that different degrees of activity-dependent calcium loading might play a crucial role for selective neurodegeneration (Surmeier et al., 2017). Given that the lateral SN is the most vulnerable DA region in PD (Damier et al., 1999; Gibb and Lees, 1991), we believe that the high *in vivo* burstiness of lateral SN DA neurons might be an attractive new target for protective intervention.

In contrast, we were surprised to find that mSN DA neurons projecting to dorsomedial striatum virtually showed no *in vivo* burst firing. This implies that K-ATP channel dependent burst mechanisms, which we previously identified to be selective for the medial SN (Schiemann et al., 2012), are operative in lateral shell-projecting rather than dorsomedial striatum-projecting DA neurons in this region. The mechanism for

bioRxiv preprint doi: https://doi.org/10.1101/624700; this version posted May 2, 2019. The copyright holder for this preprint (which was not certified by peer review) is the author/funder. All rights reserved. No reuse allowed without permission.

this region-specific absence of bursting are currently unknown but might be highly relevant given that selective dysregulation in DA projections to dorsomedial striatum has been associated with schizophrenia (Kegeles et al., 2010; McCutcheon et al., 2019).

Finally, our study gives further support to the idea that mesolimbic DA neurons projecting to medial versus lateral shell of accumbens constitute two parallel pathways. Recent studies highlighted the differential functional roles of these DA projections, as well as their distinct circuit affiliations (de Jong et al., 2019; Lammel et al., 2012; Yang et al., 2018). Our frequency data suggest that these two DA projections operate at different baseline excitation/inhibition (E/I) setpoints *in vivo*. In particular, medial shell projecting DA neurons, which displayed high intrinsic excitability associated with sustained high frequency firing *in vitro* (Lammel et al., 2008), discharged *in vivo* at a lower rate, which might be indicative for a higher degree of tonic net inhibition. Based on the systematic firing differences between these two mesolimbic DA subpopulations, that intermingle mainly within the VTA, it will crucial for future work in awake animals to disentangle them.

In summary, we have provided a refined source-target functional *in vivo* topography of midbrain DA neurons, which we believe will facilitate our understanding of dopamine neuron diversity in health and disease.

bioRxiv preprint doi: https://doi.org/10.1101/624700; this version posted May 2, 2019. The copyright holder for this preprint (which was not certified by peer review) is the author/funder. All rights reserved. No reuse allowed without permission.

Figure Legends

Figure 1 1000-fold reduction of conventional FG-concentrations leads to intact FG-labelled DA neurons *in vivo*

(A) Confocal images of a dilution series of Fluorogold/ACSF injections. (Top panel, 1st row) merged images of injections sites (4x magnification) in the dorsal striatum with TH in green and FG in blue. (2nd and 3rd row) 10x images of retrogradely traced neurons (FG black in the 2nd row and blue in the 3rd row) in the midbrain (TH green) at bregma -3.16mm (10x magnification).

(Bottom panel) Images of retrogradely traced SN DA neurons at higher magnification (60x; FG black in the 1st row and blue in the 3rd row, TH green). Note that 0.002% FG constitutes the lowest detectable concentration.

(B) Use of FG-Antibody facilitates identification of FG-labelled neurons after 0.002% FG/ACSF infusion. Note the increased detectability in comparison to the intrinsic FG signal after 0.002% infusion of FG (Fig 1A column four).

Figure 2 Experimental design and electrophysiological data of control neuron and FG-labelled SN DA neuron

(A) Experimental design for FG-labelled DA dataset. Control DA neurons were recorded in untreated mice (only “Day 7”).

(B1, C1) spontaneous *in vivo* extracellular single-unit activities of a representative control DA lSN neuron (B) and a representative FG-labelled DLS-projecting DA lSN neuron (C), shown as 10s of original recording traces (scale bar: 0.2mV, 1s).

(B2, C2) 30s raster plots (scale bar: 1s).

(B3, C3) ISI-distributions. Inset, averaged AP waveform showing biphasic extracellular action potentials in high resolution (scale bar: 0.2mV, 1ms).

(B4, C4) Confocal images of extracellularly recorded and juxtacellularly labelled neurons, the location of the neurons in the lSN at bregma -3.08mm is shown in the bottom right image.

Note the similarities in mean frequency, regularity, firing pattern, AP waveform and anatomical location.

Figure 3 Retrograde tracing with highly-diluted (0.002%) fluorogold prevents perturbation of *in vivo* electrophysiological properties of identified nigrostriatal dopamine neurons

(A) Anatomical mapping of all extracellularly recorded and juxtacellularly labelled neurons (projected to bregma -3.16mm; control in black, FG-labelled in green). Note the anatomical overlap of recorded DA populations in the lSN. Insert, FG-injection site in DLS (FG in blue, TH in green).

(B-F) Scatter dot-plots (line at median) showing no significant differences in firing frequency (Hz), coefficient of variation (%), kurtosis and skewness of the ISI-distributions, GLO-based firing pattern (all B), normalized AP waveform, AP duration (ms), relative AP trough (all C), pauses per minute, pause duration (s) (both D), SFB (%), SFB contingency (% of neurons > and <5% SFB) (both E), bursts per minute, intraburst-frequency (Hz) (both F)

bioRxiv preprint doi: https://doi.org/10.1101/624700; this version posted May 2, 2019. The copyright holder for this preprint (which was not certified by peer review) is the author/funder. All rights reserved. No reuse allowed without permission.

Figure 4 Dorsal and ventral striatal-projecting DA neurons intermix within the mSN

(A1-D1) Injection sites for fluorescent tracing experiments injecting FG into the DLS (A1; bregma +0.86mm), DMS (B1; bregma +0.74mm), lNAcc (C1; bregma +0.86mm), mNacc (D1; bregma +1.54mm). (Left images) merged TH-(green) and FG-(blue) signals. (Right images) FG mono.

(A2-D2) location of retrogradely traced DA neurons (accumulated from n=3 animals) at a rostral (-3.16mm) and a caudal (-3.64mm) midbrain section, shown as colored heat maps. DLS-projecting DA neurons (A2) are shown in green, DMS-projecting DA neurons (B2) in cyan, lNAcc-projecting DA neurons (C2) in magenta, mNAcc-projecting DA neurons (D2) in orange. The boarder between lSN and mSN is indicated with a yellow dotted line. Note that DLS-projecting DA neurons are located throughout the mediolateral extent of the SN (A2) and that the mSN is a substantial midbrain source area for three mayor projection-defined systems (A2-C2).

(E1) Local cell population matrix (%, average of three animals). Note that the lSN, PBP, PN and IF are populated mainly by one projection-defined population each (lSN - DLS, PBP - lNAcc, PN and IF - mNAcc). However, the mSN is a region of overlap of DLS-, DMS- and lNAcc- projecting DA neurons.

(F1) Projection population matrix (%, average of three animals). Note that the DLS receives dopaminergic input from both SN source areas (lSN and mSN). On the other side, DMS mainly receives input from the mSN, lNAcc from PBP, mNAcc from PN.

(E2) Shared sources & distinct targets. The mSN is a region of overlap of three different projection target-defined systems (DLS, DMS and lNAcc). The VTA harbors both the mNAcc and lNAcc projection system.

(F2) Distinct sources & shared target. The DLS receives dopaminergic input from two distinct midbrain source areas (lSN and mSN).

bioRxiv preprint doi: https://doi.org/10.1101/624700; this version posted May 2, 2019. The copyright holder for this preprint (which was not certified by peer review) is the author/funder. All rights reserved. No reuse allowed without permission.

Figure 5 High *in vivo* burstiness in lateral compared to medial DLS-projecting SN DA neurons

(A1, B1) spontaneous *in vivo* extracellular single-unit activities of a representative DLS-projecting DA neuron located in the lSN (A1) and a representative DLS-projecting DA neuron located in the mSN (B1), shown as 10s of original recording traces (scale bar: 0.2mV, 1s). Note the differences in burstiness.

(A2, B2) 30s raster plots (scale bar: 1s).

(A3, B3) ISI-distributions. Note the presence of ISIs below 80ms and 160ms indicating bursts in A3 in contrast to B3. Inset, averaged AP waveform showing biphasic extracellular action potentials in high resolution (scale bar: 0.2mV, 1ms).

(A4, B4) Confocal images of retrogradely traced, extracellularly recorded and juxtacellularly labelled DA neurons, the location of the neurons is displayed in the bottom right image.

(C) Anatomical mapping of all extracellularly recorded and juxtacellularly labelled neurons (projected to bregma -3.16mm; DLS-lSN in green, DLS-mSN in red). Insert, FG-injection site in DLS (FG in blue, TH in green).

(D) Cumulative SFB distribution histograms (dotted line at SFB=5% threshold) and bar graphs of SFB contingencies (% of neurons > and <5% SFB) showing significant differences in burstiness. Note that no DLS-projecting DA neurons located in the mSN displayed a SFB above 5%.

(E) Linear discriminant analysis of DLS-projecting DA neurons located either in the mSN or lSN. (Right Picture) Mapping of correctly- vs incorrectly-classified DLS-projecting DA neurons located in mSN or lSN.

Figure 6 Functional segregation of *in vivo* electrophysiological properties mSN DA neurons with distinct axonal projections

(A1, B1) spontaneous *in vivo* extracellular single-unit activities of a representative DS-projecting DA neuron located in the mSN (A1) and a representative lNAcc-projecting DA neuron located in the mSN (B1), shown as 10s of original recording traces (scale bar: 0.2mV, 1s). Note the differences in bursting.

(A2, B2) 30s raster plots (scale bar: 1s).

(A3, B3) ISI-distributions. Note the presence of ISIs below 80ms and 160ms indicating bursts in B3 in contrast to A3. Inset, averaged AP waveform showing biphasic extracellular action potentials in high resolution (scale bar: 0.2mV, 1ms).

(A4, B4) Confocal images of retrogradely traced, extracellularly recorded and juxtacellularly labelled DA neurons, the location of the neurons is displayed in the bottom right image.

(C) Anatomical mapping of all retrogradely traced, extracellularly recorded and juxtacellularly labelled neurons (projected to bregma -3.16mm; DS-lSN in blue, lNAcc-mSN in magenta). Insert, FG-injection sites in DMS, DLS and lNAcc (FG in blue, TH in green).

(D) Cumulative SFB distribution histograms (dotted line at SFB=5% threshold) and bar graphs of SFB contingencies (% of neurons > and <5% SFB) showing significant differences in burstiness.

(E) Cumulative distribution histograms and bar graphs of pauses per minute showing significant differences.

(F) Scatter dot-plots showing significant differences in kurtosis and skewness of the ISI-distributions.

(G) Linear discriminant analysis of DA mSN neurons projecting either to DLS/DMS or lNAcc. 70.8% of neurons were classified correctly based on skewness of the ISI-

bioRxiv preprint doi: https://doi.org/10.1101/624700; this version posted May 2, 2019. The copyright holder for this preprint (which was not certified by peer review) is the author/funder. All rights reserved. No reuse allowed without permission.

distribution, AP duration, repolarization speed and the precision of spiking ($\log(\sigma_2)$) when randomly bisecting the data 1000 times. When the whole data set was used, 84.4% of neurons were classified correctly.

(Right Picture) Mapping of correctly- vs incorrectly-classified DA mSN neurons projecting to DS or lNAcc.

Figure 7 DA neurons projecting to medial or lateral shell of the nucleus accumbens display distinct *in vivo* firing rates

(A1, B1) spontaneous *in vivo* extracellular single-unit activities of a representative lNAcc-projecting DA neuron located in the mSN (A1) and a representative mNAcc-projecting DA neuron located in the VTA (B1), shown as 10s of original recording traces (scale bar: 0.2mV, 1s). Note the differences in firing frequency.

(A2, B2) 30s raster plots (scale bar: 1s). Blue lines indicate pauses. Note the differences in pause duration.

(A3, B3) ISI-distributions. Note the differences in overall shape and maximal ISIs. Inset, averaged AP waveform showing biphasic extracellular action potentials in high resolution (scale bar: 0.2mV, 1ms).

(A4, B4) Confocal images of retrogradely traced, extracellularly recorded and juxtacellularly labelled DA neurons, the location of the neurons is displayed in the bottom right image.

(C) Anatomical mapping of all extracellularly recorded and juxtacellularly labelled neurons (projected to bregma -3.16mm; lNAcc in magenta, mNAcc in orange). Insert, FG-injection sites in lNAcc and mNAcc (FG in blue, TH in green).

(D) Scatter dot-plots (line at median) showing significant differences in firing frequency (Hz) and pause duration (s).

bioRxiv preprint doi: https://doi.org/10.1101/624700; this version posted May 2, 2019. The copyright holder for this preprint (which was not certified by peer review) is the author/funder. All rights reserved. No reuse allowed without permission.

Figure 8 Midbrain dopamine neurons with distinct source-target topographies display functional *in vivo* firing differences

(A) Diagram of the organization of distinct midbrain DA subtypes defined by their source-target topography. Single midbrain source areas and striatal target areas are colored individually (midbrain: lSN red, mSN yellow, PBP brown, PN light green; striatum: DLS green, DMS cyan, lNAcc magenta, mNAcc orange). Distinct subtypes are illustrated with a circle in the midbrain source area and an arrow to the projection target area.

(B) Comparisons of *in vivo* activities of distinct source-target topography defined DA subtypes

bioRxiv preprint doi: https://doi.org/10.1101/624700; this version posted May 2, 2019. The copyright holder for this preprint (which was not certified by peer review) is the author/funder. All rights reserved. No reuse allowed without permission.

Materials and Methods

Mice

Male C57Bl6/N mice (Charles River Laboratories) were used for the study. Mice were between 11-16 weeks old, group housed and maintained on a 12-hour light-dark cycle. All experiments and procedures involving mice were approved by the German Regierungspräsidium Darmstadt (V54-19c20/15-F40/28).

Retrograde Fluorogold tracing

Mice were anesthetized using isoflurane (AbbVie, North Chicago, USA; induction 3.5%, maintenance 0.8–1.4% in O2, 0.35 l/min) and placed in a stereotaxic frame (Kopf, Tujunga, CA, USA). Eye cream (Vidisic, Dr Mann Pharma, Berlin, Germany) was applied on the eyes to prevent dehydration of the cornea. Lidocaine gel (Astra Zeneca, Wedel, Germany) was used as a local analgesic at the incision site. Rectal temperature (33–36°C), and respiration (1–2 Hz) were constantly monitored. Craniotomies were performed using a stereotaxic drill (0.75 mm diameter) to target the dorsal striatum (DS; bregma: 0.86 mm, lateral: 2.0 mm, ventral: 2.8 mm), dorsolateral striatum (DLS; bregma: 0.86 mm, lateral: 2.2 mm, ventral: 2.6 mm), dorsomedial striatum (DMS; bregma: 0.74 mm, lateral: 1.4 mm, ventral: 2.6 mm), nucleus accumbens (NAcc) lateral shell (lNAcc; bregma: 0.86 mm, lateral: 1.75 mm, ventral: 4.5 mm), NAcc medial shell (mNAcc; bregma: 1.54 mm, lateral: 0.7 mm, ventral: 4.25 mm) and medial prefrontal cortex (mPFC; prelimbic nucleus (PrL; bregma: 1.98 mm, lateral: 0.3 mm, ventral: 1.5 mm) and infralimbic nucleus (IL; bregma: 1.98 mm, lateral: 0.3 mm, ventral: 2.1 mm)). Coordinates were corrected according to Lammel et al. 2008.

bioRxiv preprint doi: https://doi.org/10.1101/624700; this version posted May 2, 2019. The copyright holder for this preprint (which was not certified by peer review) is the author/funder. All rights reserved. No reuse allowed without permission.

Fluorogold (FG, Fluorochrome, Denver, USA) dissolved in artificial cerebrospinal fluid (2%, 0.2%, 0.02%, 0.002%, 0.0002%, 500nl for DS-infusions, 1500nl for NAcc-infusions, 2x1000nl for mPFC-infusions) was infused either uni- or bilaterally into the target area using a micro-pump (UMP3-1, WPI, Berlin, Germany, 10*µl* nanofil syringe, 33-gauge steel needle; flow rate of 50nl/min). Post- infusion, mice were given Carprofen (Pfizer, Berlin, Germany, 4mg/kg) subcutaneously into the nape. After a 1-week recovery period, animals were either anesthetized with Pentobarbital (Merial GmbH, 1.6 g/kg) and transcardially perfused with fixative (4% paraformaldehyde, 15% picric acid in phosphate-buffered saline, pH 7.4) for histological analysis, or used for *in vivo* extracellular recordings. The perfused brains were stored in paraformaldehyde overnight and changed to a 10% sucrose/0.05% NaN3 solution for long-term storage.

In vivo electrophysiology

In vivo extracellular single-unit activities of SN and VTA neurons were recorded in untreated (Control) or post-infused (FG) mice with similar procedures as used in other studies from our lab (Schiemann et al., 2012). Briefly, mice were again anesthetized (isoflurane; induction 3.5%, maintenance 0.8–1.4% in 0.35 l/min O2) and placed into a stereotactic frame. The craniotomies were performed as described above to target the lateral SN (bregma: -3.08 mm, lateral: 1.4 mm, ventral: 3.5-4.5 mm), medial SN (bregma: -3.08 mm, lateral: 0.9 mm, ventral: 4.2-5.0 mm), VTA (bregma: -3.08 mm, lateral: 0.75 mm, ventral: 4.0-5.0 mm). Borosilicate glass electrodes (10–25 MΩ; Harvard Apparatus, Holliston, MA, USA) were made using a horizontal puller (DMZ-Universal Puller, Zeitz, Germany) and filled with 0.5 M NaCl, 10 mM HEPES (pH 7.4) and 1.5% neurobiotin (Vector Laboratories, Burlingame, CA, USA). A micromanipulator (SM-6; Luigs & Neumann, Ratingen, Germany) was used

bioRxiv preprint doi: https://doi.org/10.1101/624700; this version posted May 2, 2019. The copyright holder for this preprint (which was not certified by peer review) is the author/funder. All rights reserved. No reuse allowed without permission.

to lower the electrodes to the recording site. The single-unit activity of each neuron was recorded for at least 10 minutes at a sampling rate of 12.5 kHz (for firing pattern analyses), and then for another one minute at a sampling rate of 20 kHz (for the fine analysis of AP waveforms). Signals were amplified 1000x (ELC-03M; NPI electronics, Tamm, Germany), notch- and bandpass-filtered 0.3–5000 Hz (single-pole, 6 dB/octave, DPA-2FS, NPI electronics) and recorded on a computer with an EPC-10 A/D converter (Heka, Lambrecht, Germany). Simultaneously, the signals were displayed on an analog oscilloscope and an audio monitor (HAMEG Instruments CombiScope HM1508; AUDIS-03/12M NPI electronics). Midbrain DA neurons were initially identified by their broad biphasic AP (> 1.2 ms duration) and slow frequency (1–8 Hz) (Grace & Bunney, 1984; Ungless et al., 2004). AP duration was determined as the interval between the start of initial upward component and the minimum of following downward component.

Juxtacellular labeling of single neurons

In order to identify the anatomical location and neurochemical identity of the recorded neurons, they were labeled post-recording with neurobiotin using the juxtacellular *in vivo* labeling technique (Pinault, 1996). Microiontophoretic currents were applied (1–10 nA positive current, 200ms on/off pulse, ELC-03M, NPI Electronics) via the recording electrode in parallel to the monitoring of single-unit activity. Labeling was considered successful when the firing pattern of the neuron was modulated during current injection (i.e., increased activity during on-pulse and absence of activity in the off-pulse) and the process was stable for at least 20s followed by the recovery of spontaneous activity. This procedure allowed for the exact mapping of the recorded DA neuron within the SN and VTA subnuclei (Franklin and Paxinos, 2008) using

bioRxiv preprint doi: https://doi.org/10.1101/624700; this version posted May 2, 2019. The copyright holder for this preprint (which was not certified by peer review) is the author/funder. All rights reserved. No reuse allowed without permission.

custom written scripts in Matlab 2016a (MathWorks, Natick, MA, USA), combined with neurochemical identification using TH immunostaining.

Immunohistochemistry

Following *in vivo* recordings, the animals were transcardially perfused as described previously. Fixed brains were sectioned into 60µm (midbrain) or 100µm (forebrain) coronal sections using a vibrating microtome (VT1000S, Leica). Sections were rinsed in PBS and then incubated (in blocking solution (0.2 M PBS with 10% horse serum, 0.5% Triton X-100, 0.2% BSA). Afterwards, sections were incubated in in carrier solution (room temperature, overnight) with the following primary antibodies: polyclonal guinea pig anti-tyrosine hydroxylase (TH; 1:1000; Synaptic Systems), monoclonal mouse anti-TH (1:1000; Millipore), polyclonal rabbit anti-TH (1:1000; Synaptic Systems), polyclonal rabbit anti-FG (1:1000, Fluorochrome), monoclonal mouse anti-calbindin (CB; 1:1000; Swant). In sequence, sections were again washed in PBS and incubated (room temperature, overnight) with the following secondary antibodies: goat anti-guinea pig 488, goat anti-guinea pig 647, goat anti-rabbit 568, goat anti-rabbit 488, goat anti-mouse 647, goat anti-mouse 488 (all 1:750; Life Technologies). Streptavidin AlexaFluor-568 and Streptavidin AlexaFluor-488 (both 1:1000; Invitrogen) were used for identifying neurobiotin-filled cells. Sections were then rinsed in PBS and mounted on slides with fluorescent mounting medium (Vectashield, Vector Laboratories).

Confocal analysis and FG detection

Multilabeling fluorescent immunostainings of recorded, juxtacellularly filled and retrogradely traced neurons were analyzed using a laser-scanning microscope

bioRxiv preprint doi: https://doi.org/10.1101/624700; this version posted May 2, 2019. The copyright holder for this preprint (which was not certified by peer review) is the author/funder. All rights reserved. No reuse allowed without permission.

(Nikon Eclipse90i, Nikon GmbH). NIS-Elements C program (Nikon software) was used to acquire and export images. Low magnification images of the forebrain injection sites were acquired with a 4x objective. Overview images of the midbrain were acquired with 10x or 20x objectives. High magnification images of traced and juxtacellularly labeled neurons were acquired with a 60x oil immersion objective. For FG-labelling detection, confocal settings differed between neurons that did not undergo FG immunohistochemistry (intrinsic FG signal) and neurons that did undergo FG immunohistochemistry. Identical confocal settings were chosen within each group. For semiquantitative analysis of both intrisic and immuno-FG signals in the soma of juxtacellularly labeled SN and VTA DA neurons, we determined the mean intrinsic FG signal intensities of TH-negative background regions and TH-positive regions-of-interests in the midbrain using ImageJ software (http://rsbweb.nih.gov/ij/). TH-negative nuclei were subtracted from the background. For intrinsic FG signals, a neuron was identified as FG- labeled if FG signals in the ROI were higher than the mean background intensity + 2*SD of the mean background. For immuno-FG signals, neurons were identified as FG-positive if there were >5 FG-positive marks after thresholding images at mean background + 10*SD of the mean background. Also, >95% of retrogradely FG-3-labeled neurons in both the SN and the VTA were TH-positive i.e. dopaminergic (99.23% of DLS-projecting midbrain neurons, 99.19% of DMS-projecting midbrain neurons, 98.57% of lNAcc-projecting neurons, 96.34% of mNAcc-projecting neurons).

Mapping and anatomical quantification of projection-defined DA neuron subtypes

bioRxiv preprint doi: https://doi.org/10.1101/624700; this version posted May 2, 2019. The copyright holder for this preprint (which was not certified by peer review) is the author/funder. All rights reserved. No reuse allowed without permission.

In order to map projection-defined DA subtypes in the midbrain, three animals in each group (DMS, DLS, lNAcc, mNAcc) were infused with FG and processed after a 1-week survival period. After TH-, FG- and Calbindin-immunohistochemistry was performed, 10x and 20x z-stack images of 60µm midbrain sections were acquired and every 2nd image was used for analyses. To illustrate the anatomical segregation of different projection-defined subtypes, images from 10x z-stack images were flattened into single maximum intensity projections using Image J. Sections were defined according to their distance relative to bregma and neuroanatomical landmarks using (Franklin and Paxinos, 2008). Sections at the same bregma were aligned using ImageJ FIJI and merged. Image brightness was adjusted relative to maximum peak, the background was subtracted (rolling ball radius=10), a Gaussian blur filter was employed (sigma=5), and a colored heat map was created using ImageJ plugin by Samuel Péan (http://imagejdocu.tudor.lu/doku.php?id=plugin:analysis:heatmap_histogram:start). The heat map image was then overlaid on the corresponding stereotactic map figures (Franklin and Paxinos, 2008).

For the quantification of projection-defined DA neuronal cell populations, 20x z-stack images of 60µm thick midbrain sections were taken. FG-positive, FG- and TH-copositive and FG-, TH- and CB-copositive neurons were counted manually with ImageJ cell counter by Kurt De Vos (https://imagej.nih.gov/ij/plugins/cell-counter.html). For quantification, either absolute accumulated numbers of neurons (n=3 animals) were presented or the average percentage of neurons either located in a distinct midbrain area or projecting to a distinct target area.

Statistical Analysis

bioRxiv preprint doi: https://doi.org/10.1101/624700; this version posted May 2, 2019. The copyright holder for this preprint (which was not certified by peer review) is the author/funder. All rights reserved. No reuse allowed without permission.

Spike train analyses

Spike timestamps were extracted by thresholding above noise levels with IGORPRO 6.02 (WaveMetrics, Lake Oswego, OR, USA). Firing pattern properties such as mean frequency, coefficient of variation (CV) and bursting measures were analyzed using custom scripts in Matlab (R2016b). In order to estimate burstiness and intra-burst properties, we used the burst detection methods described in Grace & Bunney (1984). Only cells with estimated bursts were included for the intraburst-statistics. For intraburst-frequency analysis, the average of mean intraburst-frequencies of all bursts in a spiketrain were calculated. Pauses were detected using a custom version of the Tukey outlier identification algorithm (Tukey, 1977). This method relies on setting a non-parametric pause threshold that is adjusted to each cell but applied across the entire spike train. The pause threshold $Pthr$ is the 75% quantile $q3$ of the ISI distribution, added to a factor *w* (set as 3 in this study) multiplied by the interquartile range: $Pthr=q3+3*(q3-q1)$. Also, pauses after bursts are excluded as they putatively could be of non-synaptic origin.

For analysis of general firing patterns, autocorrelation histograms (ACH) were plotted using custom Matlab scripts. As described before (Schiemann et al., 2012), we used established criteria for classification of *in vivo* firing patterns based on visual inspection of autocorrelograms: single spike-oscillatory (“Pacemaker”; ≥3 equidistant peaks with decreasing amplitudes), single spike-irregular (“irregular”; <3 peaks, increasing from zero approximating a steady state), bursty-irregular (“irregularly bursty”; narrow peak with steep increase at short ISIs) and bursty-oscillatory (“regularly bursty”; narrow peak reflecting fast intraburst ISIs followed by clear trough and repetitive broader peaks).

For a quantitative description of firing patterns, we fitted a stochastic model called Gaussian Locking to a free Oscillator (GLO; Bingmer et al., 2011, Schiemann et al.,

bioRxiv preprint doi: https://doi.org/10.1101/624700; this version posted May 2, 2019. The copyright holder for this preprint (which was not certified by peer review) is the author/funder. All rights reserved. No reuse allowed without permission.

2012) to the spike trains. The GLO mainly includes the four parameters mean period and variability of oscillation, burst size and precision of spike locking to the oscillation (σ_2). In order to fit the GLO, we first applied a multiple filter test for rate stationarity (Messer et al., 2014) to identify the longest sections with approximately constant firing rate. The GLO was then used to classify this longest stationary phase into single spike oscillatory, irregular single spike, etc. The GLO analysis was performed using the statistical analysis package R (www.r-project.org).

For AP duration analysis, high-resolution recordings of at least 10 APs were aligned, averaged and the interval between the start of the initial upward component and the minimum of the following downward component was measured using IGORPRO. In order to analyze the relative AP trough, aligned and averaged APs of single neurons were normalized to peak amplitude=1mV and the trough was measured using IGORPRO.

Numerical data is represented as scatter plots with a line on the median. Categorical data is represented as stacked bar graphs. To investigate the assumption of normal distribution, we performed the single-sample Kolmogorov-Smirnov test. Because, in general, the normality assumption was rejected, comparisons were performed with the nonparametric Mann–Whitney-Test. Categorical parameters such as GLO-based firing pattern and SFB contingency were analyzed with the Chi-squared test. Statistical significance level was set to $p < 0.05$. All data values are presented as means ± SEM. Statistical tests were made using GraphPad Prism 6 (GraphPad Software, San Diego, CA, USA).

Linear Discriminant Analysis

We applied linear discriminant analysis (LDA) to determine whether different projection-defined DA neuron subpopulations could be reliably discriminated based on their firing patterns alone. In a multidimensional data set with two or more specified groups, the LDA finds the direction that optimally separates the groups. In order to identify the set of variables contributing to this discrimination, we used the following cross validation technique: For every possible subset S_j of the set of all variables (i.e., the four GLO parameters, the mean spike frequency, the CV, the SFB, the skewness and kurtosis of the interspike intervals, the burst rate, the number of estimated pauses, the AP duration and the relative AP through), we performed the following analysis: we used 1000 random divisions of the data in two equally sized groups A and B. For every division, we performed LDA on A and predicted the group affiliations of B, and vice versa. The mean percentage of correct predictions in A and B, averaged across all 1000 random divisions, is called the predictive power of the model with variable set S_j and denoted by M_j. The maximal predictive power is then given by $\max_j M_j$ and the corresponding subset S_j is called the best subset.

In order to investigate statistical significance of the maximal predictive power, we used a permutation test, performing the same analysis with 1000 randomly permuted data sets, in which the two groups were assigned randomly. Statistical significance was then assessed by deriving the percentage of these analyses of permuted data sets – as specified in the results – which yielded a maximal predictive power as large as or larger than the observed. In case of statistical significance, we also give the percentage of correct categorizations for the respective subset S_j when performing LDA on the whole data set.

bioRxiv preprint doi: https://doi.org/10.1101/624700; this version posted May 2, 2019. The copyright holder for this preprint (which was not certified by peer review) is the author/funder. All rights reserved. No reuse allowed without permission.

Acknowledgements

This study was supported by research grants to J.R. (NIH Grant R01DA041705, DFG CRC 1080 and a Fellowship by the Gutenberg Research College, University Mainz) and to G.S. by the DFG Priority Program 1665 (SCHN 1370/02-1). N.F. is a MD/PhD candidate at TransMed, Gutenberg University Mainz. We thank Beatrice Fischer and Jasmine Sonntag for technical assistance.

Author Contributions

N.F. established the highly-diluted fluorogold retrograde labelling protocol and carried out most experiments and analysis; he also co-wrote the manuscript. J.R. supervised N.F, designed the study and wrote the manuscript. K.M.C. provided Matlab scripts for anatomical mapping and supported data analysis. J.S. supported data analysis. M.S. and L.K. assisted *in vivo* recording and labelling techniques. S.A. and G.S. designed and carried out GLO-based modelling and linear discriminant analysis.

Declaration of Interests

The authors declare no competing interests.

bioRxiv preprint doi: https://doi.org/10.1101/624700; this version posted May 2, 2019. The copyright holder for this preprint (which was not certified by peer review) is the author/funder. All rights reserved. No reuse allowed without permission.

References

Beier, K.T., Gao, X.J., Xie, S., DeLoach, K.E., Malenka, R.C., and Luo, L. (2019). Topological Organization of Ventral Tegmental Area Connectivity Revealed by Viral-Genetic Dissection of Input-Output Relations. Cell Rep *26*, 159-167 e156.

Beier, K.T., Steinberg, E.E., DeLoach, K.E., Xie, S., Miyamichi, K., Schwarz, L., Gao, X.J., Kremer, E.J., Malenka, R.C., and Luo, L. (2015). Circuit Architecture of VTA Dopamine Neurons Revealed by Systematic Input-Output Mapping. Cell *162*, 622-634.

Berke, J.D. (2018). What does dopamine mean? Nat Neurosci *21*, 787-793.

Bjorklund, A., and Dunnett, S.B. (2007). Dopamine neuron systems in the brain: an update. Trends Neurosci *30*, 194-202.

Cao, J.L., Covington, H.E., 3rd, Friedman, A.K., Wilkinson, M.B., Walsh, J.J., Cooper, D.C., Nestler, E.J., and Han, M.H. (2010). Mesolimbic dopamine neurons in the brain reward circuit mediate susceptibility to social defeat and antidepressant action. J Neurosci *30*, 16453-16458.

Chaudhury, D., Walsh, J.J., Friedman, A.K., Juarez, B., Ku, S.M., Koo, J.W., Ferguson, D., Tsai, H.C., Pomeranz, L., Christoffel, D.J.*, et al.* (2013). Rapid regulation of depression-related behaviours by control of midbrain dopamine neurons. Nature *493*, 532-536.

Chuhma, N., Mingote, S., Yetnikoff, L., Kalmbach, A., Ma, T., Ztaou, S., Sienna, A.C., Tepler, S., Poulin, J.F., Ansorge, M.*, et al.* (2018). Dopamine neuron glutamate cotransmission evokes a delayed excitation in lateral dorsal striatal cholinergic interneurons. Elife *7*.

Cohen, J.Y., Haesler, S., Vong, L., Lowell, B.B., and Uchida, N. (2012). Neuron-type-specific signals for reward and punishment in the ventral tegmental area. Nature *482*, 85-88.

da Silva, J.A., Tecuapetla, F., Paixao, V., and Costa, R.M. (2018). Dopamine neuron activity before action initiation gates and invigorates future movements. Nature *554*, 244-248.

Damier, P., Hirsch, E.C., Agid, Y., and Graybiel, A.M. (1999). The substantia nigra of the human brain. II. Patterns of loss of dopamine-containing neurons in Parkinson's disease. Brain *122 (Pt 8)*, 1437-1448.

Dautan, D., Souza, A.S., Huerta-Ocampo, I., Valencia, M., Assous, M., Witten, I.B., Deisseroth, K., Tepper, J.M., Bolam, J.P., Gerdjikov, T.V.*, et al.* (2016). Segregated cholinergic transmission modulates dopamine neurons integrated in distinct functional circuits. Nat Neurosci *19*, 1025-1033.

de Jong, J.W., Afjei, S.A., Pollak Dorocic, I., Peck, J.R., Liu, C., Kim, C.K., Tian, L., Deisseroth, K., and Lammel, S. (2019). A Neural Circuit Mechanism for Encoding Aversive Stimuli in the Mesolimbic Dopamine System. Neuron *101*, 133-151 e137.

Del Cid-Pellitero, E., and Garzon, M. (2014). Hypocretin1/orexinA-immunoreactive axons form few synaptic contacts on rat ventral tegmental area neurons that project to the medial prefrontal cortex. BMC Neurosci *15*, 105.

Dreyer, J.K., Vander Weele, C.M., Lovic, V., and Aragona, B.J. (2016). Functionally Distinct Dopamine Signals in Nucleus Accumbens Core and Shell in the Freely Moving Rat. J Neurosci *36*, 98-112.

Duvarci, S., Simpson, E.H., Schneider, G., Kandel, E.R., Roeper, J., and Sigurdsson, T. (2018). Impaired recruitment of dopamine neurons during working memory in mice with striatal D2 receptor overexpression. Nat Commun *9*, 2822.

Eshel, N., Bukwich, M., Rao, V., Hemmelder, V., Tian, J., and Uchida, N. (2015). Arithmetic and local circuitry underlying dopamine prediction errors. Nature *525*, 243-246.

Evans, R.C., Zhu, M., and Khaliq, Z.M. (2017). Dopamine Inhibition Differentially Controls Excitability of Substantia Nigra Dopamine Neuron Subpopulations through T-Type Calcium Channels. J Neurosci *37*, 3704-3720.

Fu, Y., Paxinos, G., Watson, C., and Halliday, G.M. (2016). The substantia nigra and ventral tegmental dopaminergic neurons from development to degeneration. J Chem Neuroanat *76*, 98-107.

Gibb, W.R., and Lees, A.J. (1991). Anatomy, pigmentation, ventral and dorsal subpopulations of the substantia nigra, and differential cell death in Parkinson's disease. J Neurol Neurosurg Psychiatry *54*, 388-396.

bioRxiv preprint doi: https://doi.org/10.1101/624700; this version posted May 2, 2019. The copyright holder for this preprint (which was not certified by peer review) is the author/funder. All rights reserved. No reuse allowed without permission.

Gunaydin, L.A., Grosenick, L., Finkelstein, J.C., Kauvar, I.V., Fenno, L.E., Adhikari, A., Lammel, S., Mirzabekov, J.J., Airan, R.D., Zalocusky, K.A.*, et al.* (2014). Natural neural projection dynamics underlying social behavior. Cell *157*, 1535-1551.

Haber, S.N. (2014). The place of dopamine in the cortico-basal ganglia circuit. Neuroscience *282*, 248-257.

Hamid, A.A., Pettibone, J.R., Mabrouk, O.S., Hetrick, V.L., Schmidt, R., Vander Weele, C.M., Kennedy, R.T., Aragona, B.J., and Berke, J.D. (2016). Mesolimbic dopamine signals the value of work. Nat Neurosci *19*, 117-126.

Howe, M.W., and Dombeck, D.A. (2016). Rapid signalling in distinct dopaminergic axons during locomotion and reward. Nature *535*, 505-510.

Howe, M.W., Tierney, P.L., Sandberg, S.G., Phillips, P.E., and Graybiel, A.M. (2013). Prolonged dopamine signalling in striatum signals proximity and value of distant rewards. Nature *500*, 575-579.

Jin, X., and Costa, R.M. (2010). Start/stop signals emerge in nigrostriatal circuits during sequence learning. Nature *466*, 457-462.

Kegeles, L.S., Abi-Dargham, A., Frankle, W.G., Gil, R., Cooper, T.B., Slifstein, M., Hwang, D.R., Huang, Y., Haber, S.N., and Laruelle, M. (2010). Increased synaptic dopamine function in associative regions of the striatum in schizophrenia. Arch Gen Psychiatry *67*, 231-239.

Keiflin, R., Pribut, H.J., Shah, N.B., and Janak, P.H. (2019). Ventral Tegmental Dopamine Neurons Participate in Reward Identity Predictions. Curr Biol *29*, 93-103 e103.

Kim, H.F., Amita, H., and Hikosaka, O. (2017). Indirect Pathway of Caudal Basal Ganglia for Rejection of Valueless Visual Objects. Neuron *94*, 920-930 e923.

Kim, H.F., Ghazizadeh, A., and Hikosaka, O. (2015a). Dopamine Neurons Encoding Long-Term Memory of Object Value for Habitual Behavior. Cell *163*, 1165-1175.

Kim, J.I., Ganesan, S., Luo, S.X., Wu, Y.W., Park, E., Huang, E.J., Chen, L., and Ding, J.B. (2015b). Aldehyde dehydrogenase 1a1 mediates a GABA synthesis pathway in midbrain dopaminergic neurons. Science *350*, 102-106.

Kishida, K.T., Saez, I., Lohrenz, T., Witcher, M.R., Laxton, A.W., Tatter, S.B., White, J.P., Ellis, T.L., Phillips, P.E., and Montague, P.R. (2016). Subsecond dopamine fluctuations in human striatum encode superposed error signals about actual and counterfactual reward. Proc Natl Acad Sci U S A *113*, 200-205.

Kordower, J.H., Olanow, C.W., Dodiya, H.B., Chu, Y., Beach, T.G., Adler, C.H., Halliday, G.M., and Bartus, R.T. (2013). Disease duration and the integrity of the nigrostriatal system in Parkinson's disease. Brain *136*, 2419-2431.

Krabbe, S., Duda, J., Schiemann, J., Poetschke, C., Schneider, G., Kandel, E.R., Liss, B., Roeper, J., and Simpson, E.H. (2015). Increased dopamine D2 receptor activity in the striatum alters the firing pattern of dopamine neurons in the ventral tegmental area. Proc Natl Acad Sci U S A *112*, E1498-1506.

Kramer, D.J., Risso, D., Kosillo, P., Ngai, J., and Bateup, H.S. (2018). Combinatorial Expression of Grp and Neurod6 Defines Dopamine Neuron Populations with Distinct Projection Patterns and Disease Vulnerability. eNeuro *5*.

Lammel, S., Hetzel, A., Hackel, O., Jones, I., Liss, B., and Roeper, J. (2008). Unique properties of mesoprefrontal neurons within a dual mesocorticolimbic dopamine system. Neuron *57*, 760-773.

Lammel, S., Lim, B.K., Ran, C., Huang, K.W., Betley, M.J., Tye, K.M., Deisseroth, K., and Malenka, R.C. (2012). Input-specific control of reward and aversion in the ventral tegmental area. Nature *491*, 212-217.

Lerner, T.N., Shilyansky, C., Davidson, T.J., Evans, K.E., Beier, K.T., Zalocusky, K.A., Crow, A.K., Malenka, R.C., Luo, L., Tomer, R.*, et al.* (2015). Intact-Brain Analyses Reveal Distinct Information Carried by SNc Dopamine Subcircuits. Cell *162*, 635-647.

Lippert, R.N., Cremer, A.L., Edwin Thanarajah, S., Korn, C., Jahans-Price, T., Burgeno, L.M., Tittgemeyer, M., Bruning, J.C., Walton, M.E., and Backes, H. (2019). Time-dependent assessment of stimulus-evoked regional dopamine release. Nat Commun *10*, 336.

Luscher, C. (2016). The Emergence of a Circuit Model for Addiction. Annu Rev Neurosci *39*, 257-276.

bioRxiv preprint doi: https://doi.org/10.1101/624700; this version posted May 2, 2019. The copyright holder for this preprint (which was not certified by peer review) is the author/funder. All rights reserved. No reuse allowed without permission.

Matsumoto, M., and Hikosaka, O. (2009). Two types of dopamine neuron distinctly convey positive and negative motivational signals. Nature *459*, 837-841.

Matsumoto, M., and Takada, M. (2013). Distinct representations of cognitive and motivational signals in midbrain dopamine neurons. Neuron *79*, 1011-1024.

Matthews, G.A., Nieh, E.H., Vander Weele, C.M., Halbert, S.A., Pradhan, R.V., Yosafat, A.S., Glober, G.F., Izadmehr, E.M., Thomas, R.E., Lacy, G.D.*, et al.* (2016). Dorsal Raphe Dopamine Neurons Represent the Experience of Social Isolation. Cell *164*, 617-631.

McCutcheon, R.A., Abi-Dargham, A., and Howes, O.D. (2019). Schizophrenia, Dopamine and the Striatum: From Biology to Symptoms. Trends Neurosci *42*, 205-220.

Menegas, W., Akiti, K., Amo, R., Uchida, N., and Watabe-Uchida, M. (2018). Dopamine neurons projecting to the posterior striatum reinforce avoidance of threatening stimuli. Nat Neurosci *21*, 1421-1430.

Menegas, W., Babayan, B.M., Uchida, N., and Watabe-Uchida, M. (2017). Opposite initialization to novel cues in dopamine signaling in ventral and posterior striatum in mice. Elife *6*.

Menegas, W., Bergan, J.F., Ogawa, S.K., Isogai, Y., Umadevi Venkataraju, K., Osten, P., Uchida, N., and Watabe-Uchida, M. (2015). Dopamine neurons projecting to the posterior striatum form an anatomically distinct subclass. Elife *4*, e10032.

Nichterwitz, S., Chen, G., Aguila Benitez, J., Yilmaz, M., Storvall, H., Cao, M., Sandberg, R., Deng, Q., and Hedlund, E. (2016). Laser capture microscopy coupled with Smart-seq2 for precise spatial transcriptomic profiling. Nat Commun *7*, 12139.

Obeso, J.A., Stamelou, M., Goetz, C.G., Poewe, W., Lang, A.E., Weintraub, D., Burn, D., Halliday, G.M., Bezard, E., Przedborski, S.*, et al.* (2017). Past, present, and future of Parkinson's disease: A special essay on the 200th Anniversary of the Shaking Palsy. Mov Disord *32*, 1264-1310.

Ogasawara, T., Nejime, M., Takada, M., and Matsumoto, M. (2018). Primate Nigrostriatal Dopamine System Regulates Saccadic Response Inhibition. Neuron *100*, 1513-1526 e1514.

Ogawa, S.K., Cohen, J.Y., Hwang, D., Uchida, N., and Watabe-Uchida, M. (2014). Organization of monosynaptic inputs to the serotonin and dopamine neuromodulatory systems. Cell Rep *8*, 1105-1118.

Parker, N.F., Cameron, C.M., Taliaferro, J.P., Lee, J., Choi, J.Y., Davidson, T.J., Daw, N.D., and Witten, I.B. (2016). Reward and choice encoding in terminals of midbrain dopamine neurons depends on striatal target. Nat Neurosci *19*, 845-854.

Patriarchi, T., Cho, J.R., Merten, K., Howe, M.W., Marley, A., Xiong, W.H., Folk, R.W., Broussard, G.J., Liang, R., Jang, M.J.*, et al.* (2018). Ultrafast neuronal imaging of dopamine dynamics with designed genetically encoded sensors. Science *360*.

Poulin, J.F., Caronia, G., Hofer, C., Cui, Q., Helm, B., Ramakrishnan, C., Chan, C.S., Dombeck, D.A., Deisseroth, K., and Awatramani, R. (2018). Mapping projections of molecularly defined dopamine neuron subtypes using intersectional genetic approaches. Nat Neurosci *21*, 1260-1271.

Saunders, A., Macosko, E.Z., Wysoker, A., Goldman, M., Krienen, F.M., de Rivera, H., Bien, E., Baum, M., Bortolin, L., Wang, S.*, et al.* (2018a). Molecular Diversity and Specializations among the Cells of the Adult Mouse Brain. Cell *174*, 1015-1030 e1016.

Saunders, B.T., Richard, J.M., Margolis, E.B., and Janak, P.H. (2018b). Dopamine neurons create Pavlovian conditioned stimuli with circuit-defined motivational properties. Nat Neurosci *21*, 1072-1083.

Schiemann, J., Schlaudraff, F., Klose, V., Bingmer, M., Seino, S., Magill, P.J., Zaghloul, K.A., Schneider, G., Liss, B., and Roeper, J. (2012). K-ATP channels in dopamine substantia nigra neurons control bursting and novelty-induced exploration. Nat Neurosci *15*, 1272-1280.

Schultz, W. (2015). Neuronal Reward and Decision Signals: From Theories to Data. Physiol Rev *95*, 853-951.

Stauffer, W.R., Lak, A., Yang, A., Borel, M., Paulsen, O., Boyden, E.S., and Schultz, W. (2016). Dopamine Neuron-Specific Optogenetic Stimulation in Rhesus Macaques. Cell *166*, 1564-1571 e1566.

bioRxiv preprint doi: https://doi.org/10.1101/624700; this version posted May 2, 2019. The copyright holder for this preprint (which was not certified by peer review) is the author/funder. All rights reserved. No reuse allowed without permission.

Steinberg, E.E., Keiflin, R., Boivin, J.R., Witten, I.B., Deisseroth, K., and Janak, P.H. (2013). A causal link between prediction errors, dopamine neurons and learning. Nat Neurosci *16*, 966-973.

Surmeier, D.J., Obeso, J.A., and Halliday, G.M. (2017). Selective neuronal vulnerability in Parkinson disease. Nat Rev Neurosci *18*, 101-113.

Tarfa, R.A., Evans, R.C., and Khaliq, Z.M. (2017). Enhanced Sensitivity to Hyperpolarizing Inhibition in Mesoaccumbal Relative to Nigrostriatal Dopamine Neuron Subpopulations. J Neurosci *37*, 3311-3330.

Tian, J., Huang, R., Cohen, J.Y., Osakada, F., Kobak, D., Machens, C.K., Callaway, E.M., Uchida, N., and Watabe-Uchida, M. (2016). Distributed and Mixed Information in Monosynaptic Inputs to Dopamine Neurons. Neuron *91*, 1374-1389.

Tiklova, K., Bjorklund, A.K., Lahti, L., Fiorenzano, A., Nolbrant, S., Gillberg, L., Volakakis, N., Yokota, C., Hilscher, M.M., Hauling, T.*, et al.* (2019). Single-cell RNA sequencing reveals midbrain dopamine neuron diversity emerging during mouse brain development. Nat Commun *10*, 581.

Tritsch, N.X., Ding, J.B., and Sabatini, B.L. (2012). Dopaminergic neurons inhibit striatal output through non-canonical release of GABA. Nature *490*, 262-266.

Tye, K.M., Mirzabekov, J.J., Warden, M.R., Ferenczi, E.A., Tsai, H.C., Finkelstein, J., Kim, S.Y., Adhikari, A., Thompson, K.R., Andalman, A.S.*, et al.* (2013). Dopamine neurons modulate neural encoding and expression of depression-related behaviour. Nature *493*, 537-541.

Vander Weele, C.M., Siciliano, C.A., Matthews, G.A., Namburi, P., Izadmehr, E.M., Espinel, I.C., Nieh, E.H., Schut, E.H.S., Padilla-Coreano, N., Burgos-Robles, A.*, et al.* (2018). Dopamine enhances signal-to-noise ratio in cortical-brainstem encoding of aversive stimuli. Nature *563*, 397-401.

Watabe-Uchida, M., Eshel, N., and Uchida, N. (2017). Neural Circuitry of Reward Prediction Error. Annu Rev Neurosci *40*, 373-394.

Watabe-Uchida, M., Zhu, L., Ogawa, S.K., Vamanrao, A., and Uchida, N. (2012). Whole-brain mapping of direct inputs to midbrain dopamine neurons. Neuron *74*, 858-873.

Wessendorf, M.W. (1991). Fluoro-Gold: composition, and mechanism of uptake. Brain Res *553*, 135-148.

Willuhn, I., Burgeno, L.M., Everitt, B.J., and Phillips, P.E. (2012). Hierarchical recruitment of phasic dopamine signaling in the striatum during the progression of cocaine use. Proc Natl Acad Sci U S A *109*, 20703-20708.

Yang, H., de Jong, J.W., Tak, Y., Peck, J., Bateup, H.S., and Lammel, S. (2018). Nucleus Accumbens Subnuclei Regulate Motivated Behavior via Direct Inhibition and Disinhibition of VTA Dopamine Subpopulations. Neuron *97*, 434-449 e434.

Zhang, S., Qi, J., Li, X., Wang, H.L., Britt, J.P., Hoffman, A.F., Bonci, A., Lupica, C.R., and Morales, M. (2015). Dopaminergic and glutamatergic microdomains in a subset of rodent mesoaccumbens axons. Nat Neurosci *18*, 386-392.

bioRxiv preprint doi: https://doi.org/10.1101/624700; this version posted May 2, 2019. The copyright holder for this preprint (which was not certified by peer review) is the author/funder. All rights reserved. No reuse allowed without permission.

Supplemental Information

Supplemental Figure 1-1 FG-labelling detection method

(A) Detection method of intrinsic FG signals. The left image shows the TH-mask (TH in green), the right image shows the FG-channel (FG in black), the TH-mask is overlaid on both images in magenta, the four intensity histograms depict the background and single neuron FG-intensity distributions with a dotted line at the threshold of labelling detection. Threshold for detection was set to Thr=mean background intensity + 2*SD of the mean background. TH-negative nuclei were subtracted from the background.

(B) Detection method of immune-FG-signal. The left image shows the TH-mask (TH in green), the middle image shows the FG-channel (FG in black), the intensity histogram displays the FG-intensity distribution of the TH-free background, the right image shows the thresholded FG-channel, the TH-mask is overlaid on all images in magenta. Here, threshold for detection was set to Thr=mean background intensity + 10*SD of the mean background.

Supplemental Figure 3-1 Comparison of *in vivo* firing properties of control and FG-labelled neurons

(A1-P1) Scatter dot-plots (line at median) and bar graphs showing no significant differences in various parameters of firing.

(A2-P2) Feature maps of respective parameters

bioRxiv preprint doi: https://doi.org/10.1101/624700; this version posted May 2, 2019. The copyright holder for this preprint (which was not certified by peer review) is the author/funder. All rights reserved. No reuse allowed without permission.

Supplemental Figure 4-1 Anatomical segregation of different DA systems in the midbrain

(A) Serial reconstruction of retrogradely traced DA neurons across the caudorostral extent of the midbrain reveals anatomical position of DA neurons projecting to DLS (green), DMS (cyan), lNAcc (magenta) and mNAcc (orange), shown as colored heat maps from rostral (bregma -2.80mm) to caudal (bregma -4.16mm).

Note the high degree of overlap in the mSN.

(B) Absolute distribution of retrogradely labelled DA neurons between the different caudorostral levels for each projection-defined system (numbers of neurons accumulated from three animals for each group), shown as stacked bar graphs with color-coding for distinct midbrain source areas.

(C) Cumulative numbers of retrogradely labelled neurons (n=3 animals) in distinct midbrain areas for each projection-defined DA system, shown as bar graphs.

(D) Cumulative numbers of retrogradely traced populations in a distinct midbrain area (average of 3 animals ± SEM). Note the heterogeneous population in the mSN in contrast to more homogene populations in lSN, PBP, PN and IF. Data is given as mean ± SEM.

Supplemental Figure 4-2 Calbindin expression of midbrain DA neurons does not co-segregate with specific axonal projections

(A) Confocal 20x images of retrogradely FG-traced midbrain DA neurons (injection site: lNAcc) costained for TH (green), FG (white) and CB (red). Note the intermingling of CB-positive and CB-negative neurons in the VTA and mSN.

bioRxiv preprint doi: https://doi.org/10.1101/624700; this version posted May 2, 2019. The copyright holder for this preprint (which was not certified by peer review) is the author/funder. All rights reserved. No reuse allowed without permission.

(B) Higher magnification (60x, 2.5 zoom) confocal images of retrogradely traced DA neurons (same section as in (A)) costained for TH (green), FG (white) and CB (red). Note the variety of TH-, FG- and CB-costaining: The circumflex (^) shows a TH- and FG-positve but CB-negative neuron. The circle (°) displays a TH-positive but FG- and CB-negative neurons. The number sign (#) presents a TH- and CB-positive but FG-negative neuron. Finally, the star (*) represents a TH-, FG- and CB-positive neuron.

(C) Accumulated numbers of retrogradely FG-labelled and CB-positive DA neurons (n=3 animals) for each projection-defined DA system through the caudorostral axis, shown as stacked bar graphs with color-coding for distinct midbrain source areas. Note the gradient of CB-expression: from low to high: DLS-DMS-lNAcc-mNAcc. Also, note the gradient on the caudorostral axis. Most CB-expressing neurons are located in the intermediate midbrain (bregma -3.52, -3.4, -3.28mm). CB-expression levels decrease at more caudal and more rostral midbrain areas.

(D) Comparison of CB-expression levels of different projection-defined DA systems. (Top graph) Accumulated numbers of retrogradely FG-labelled CB-positive DA neurons for distinct color-coded midbrain areas. (Bottom graph) Percentages of CB-positive FG-labeled DA neurons out of all FG-labelled DA neurons in distinct color-coded midbrain areas. Note that CB-expression levels for DMS- and lNAcc-projecting neurons are different overall, but similar in the mSN.

Supplemental Figure 5-1 Comparison of *in vivo* firing properties of lSN and mSN DA neurons projecting to DLS

(A1-P1) Scatter dot-plots (line at median) and bar graphs showing significant differences selectively in SFB contingency (% of > and < 5%).

(A2-P2) Feature maps of respective parameters.

bioRxiv preprint doi: https://doi.org/10.1101/624700; this version posted May 2, 2019. The copyright holder for this preprint (which was not certified by peer review) is the author/funder. All rights reserved. No reuse allowed without permission.

Supplemental Figure 6-1 **DLS and DMS-projecting DA neurons located in the mSN do not exhibit significantly different *in vivo* firing properties**

(A) Anatomical mapping of all extracellularly recorded and juxtacellularly labelled neurons (projected to bregma -3.16mm; DLS in red, DMS in cyan). Insert, FG-injection sites in the DLS and DMS (FG in blue, TH in green).

(B-F) Scatter dot-plots and bar graphs (line at median) showing no significant differences in firing frequency (Hz), coefficient of variation (%), kurtosis and skewness of the ISI-distributions, GLO-based firing pattern (all B), normalized AP waveform, AP duration (ms), relative AP trough (all C), pauses per minute, pause duration (s) (both D), SFB (%), SFB contingency (% of neurons > and <5% SFB) (both E), bursts per minute, intraburst-frequency (Hz) (both F).

Supplemental Figure 6-2 **Comparison of *in vivo* firing properties of DS and lNAcc-projecting DA mSN neurons**

(A1-P1) Scatter dot-plots (line at median) and bar graphs showing significant differences in kurtosis, skewness, SFB (%), SFB contingency (% of > and < 5%), bursts per minute, pauses per minute.

(A2-P2) Feature maps of respective parameters.

bioRxiv preprint doi: https://doi.org/10.1101/624700; this version posted May 2, 2019. The copyright holder for this preprint (which was not certified by peer review) is the author/funder. All rights reserved. No reuse allowed without permission.

Supplemental Figure 6-3 **lNAcc-projecting DA neurons located either in mSN or VTA do not exhibit significantly different *in vivo* firing properties**

(A) Anatomical mapping of all extracellularly recorded and juxtacellularly labelled neurons (projected to bregma -3.16mm; mSN in magenta, VTA in brown). Insert, FG-injection site in the DLS (FG in blue, TH in green).

(B-F) Scatter dot-plots (line at median) and bar graphs showing no significant differences in firing frequency(Hz) , coefficient of variation (%), kurtosis and skewness of the ISI-distributions, GLO-based firing pattern (all B), normalized AP waveform, AP duration (ms), relative AP trough (all C), pauses per minute, pause duration (s) (both D), SFB (%), SFB contingency (% of neurons > and <5% SFB) (both E), bursts per minute, intraburst-frequency (Hz) (both F).

Supplemental Figure 7-1 **lNAcc and mNAcc-projecting midbrain DA neurons do not exhibit significantly different *in vivo* firing properties**

(A1-P1) Scatter dot-plots (line at median) and bar graphs showing significant differences in firing frequency (Hz) and pause duration (s)

(A2-P2) Feature maps of respective parameters.

bioRxiv preprint doi: https://doi.org/10.1101/624700; this version posted May 2, 2019. The copyright holder for this preprint (which was not certified by peer review) is the author/funder. All rights reserved. No reuse allowed without permission.

Supplemental Figure 7-2 Low success rate in identifying mPFC-projecting DA neurons

(A) (top panel) FG-injection sites (0.002%, 2x1µl, 50nl/min) in PrL (bregma: 1.98mm, lateral: 0.3mm, ventral: 1.5mm) and IL (bregma: 1.98mm, lateral: 0.3mm, ventral:2.1mm) nucleus.

(bottom panel) Retrogradely FG-labelled neurons in VTA and SN

(B) Anatomical mapping of all extracellularly recorded and juxtacellularly labelled neurons in mPFC-traced mice (open red circle: TH+/FG+, open blue circle: TH+/FG-, filled blue circle: TH-)

(C1-C4) *In vivo* extracellular activity of the single mPFC-projecting midbrain DA neuron recorded, shown as 10s of original recording traces (C1; scale bar: 0.2mV, 1s) and 30s raster plots (C2; scale bar: 1s). (C3) ISI-distributions. Inset, averaged AP waveform showing biphasic extracellular action potential in high resolution (scale bar: 0.2mV, 1ms). (C4) Confocal images of extracellularly recorded and juxtacellularly labelled neuron, the location of the neuron at bregma -3.28mm is shown in the bottom right image.

Figure 1

bioRxiv preprint doi: https://doi.org/10.1101/624700; this version posted May 2, 2019. The copyright holder for this preprint (which was not certified by peer review) is the author/funder. All rights reserved. No reuse allowed without permission.

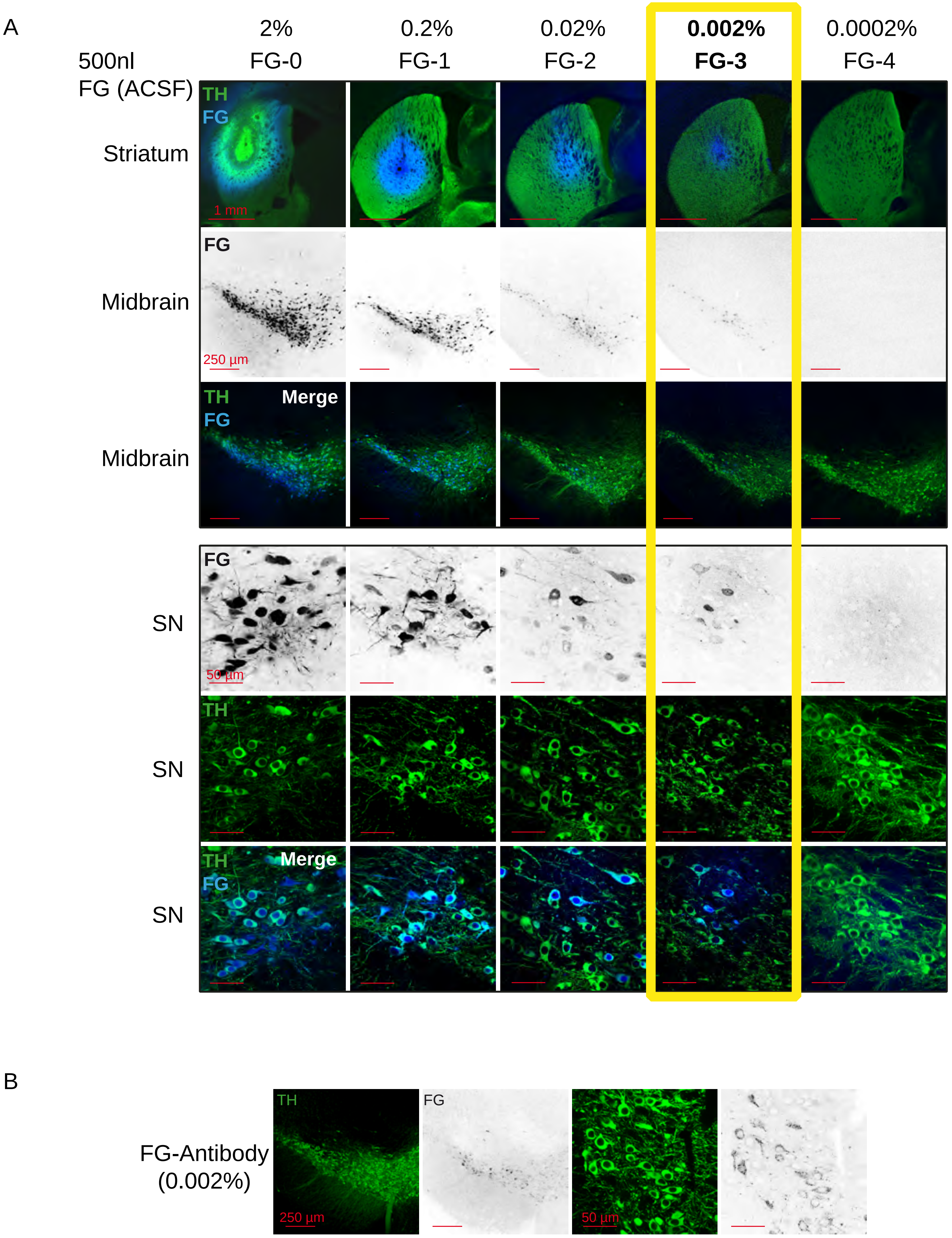

Figure 2

bioRxiv preprint doi: https://doi.org/10.1101/624700; this version posted May 2, 2019. The copyright holder for this preprint (which was not certified by peer review) is the author/funder. All rights reserved. No reuse allowed without permission.

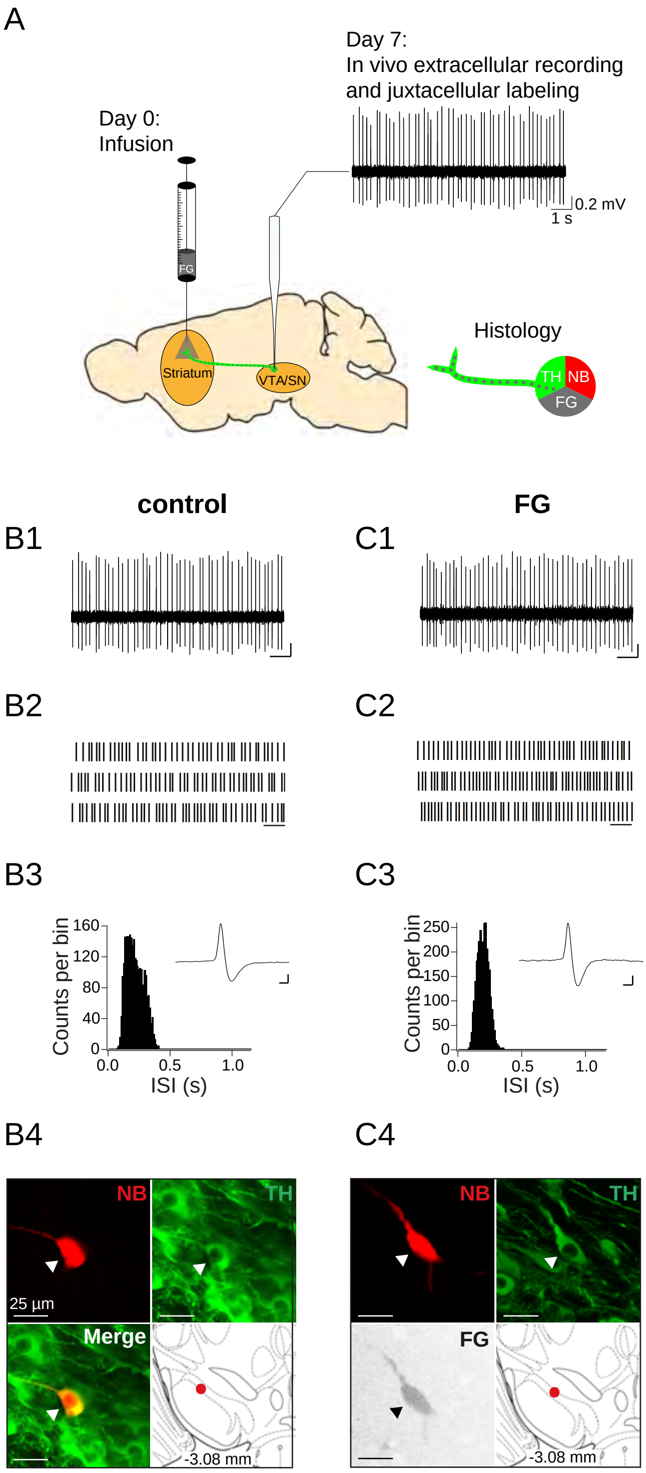

Figure 3

bioRxiv preprint doi: https://doi.org/10.1101/624700; this version posted May 2, 2019. The copyright holder for this preprint (which was not certified by peer review) is the author/funder. All rights reserved. No reuse allowed without permission.

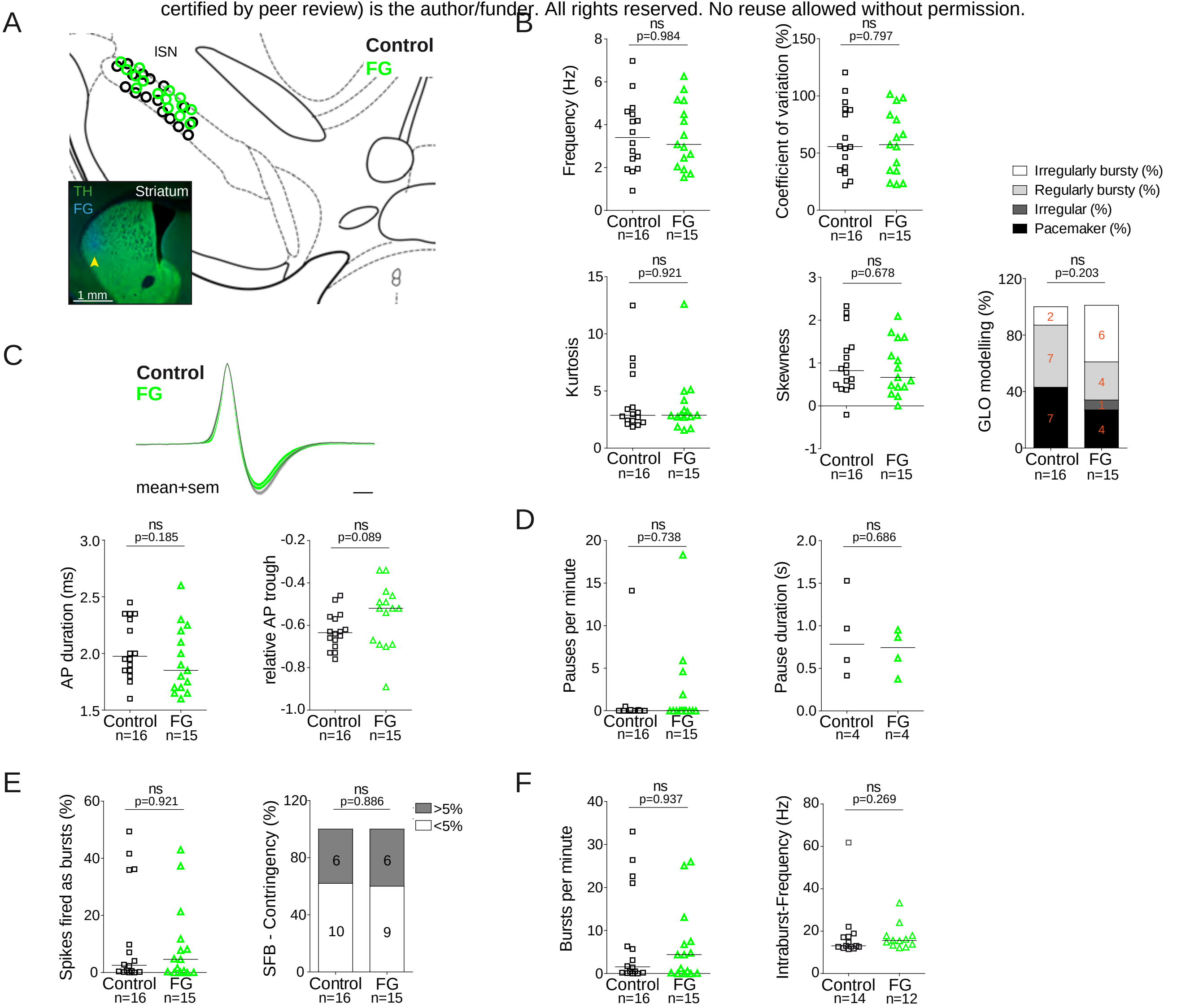

Figure 4

bioRxiv preprint doi: https://doi.org/10.1101/624700; this version posted May 2, 2019. The copyright holder for this preprint (which was not certified by peer review) is the author/funder. All rights reserved. No reuse allowed without permission.

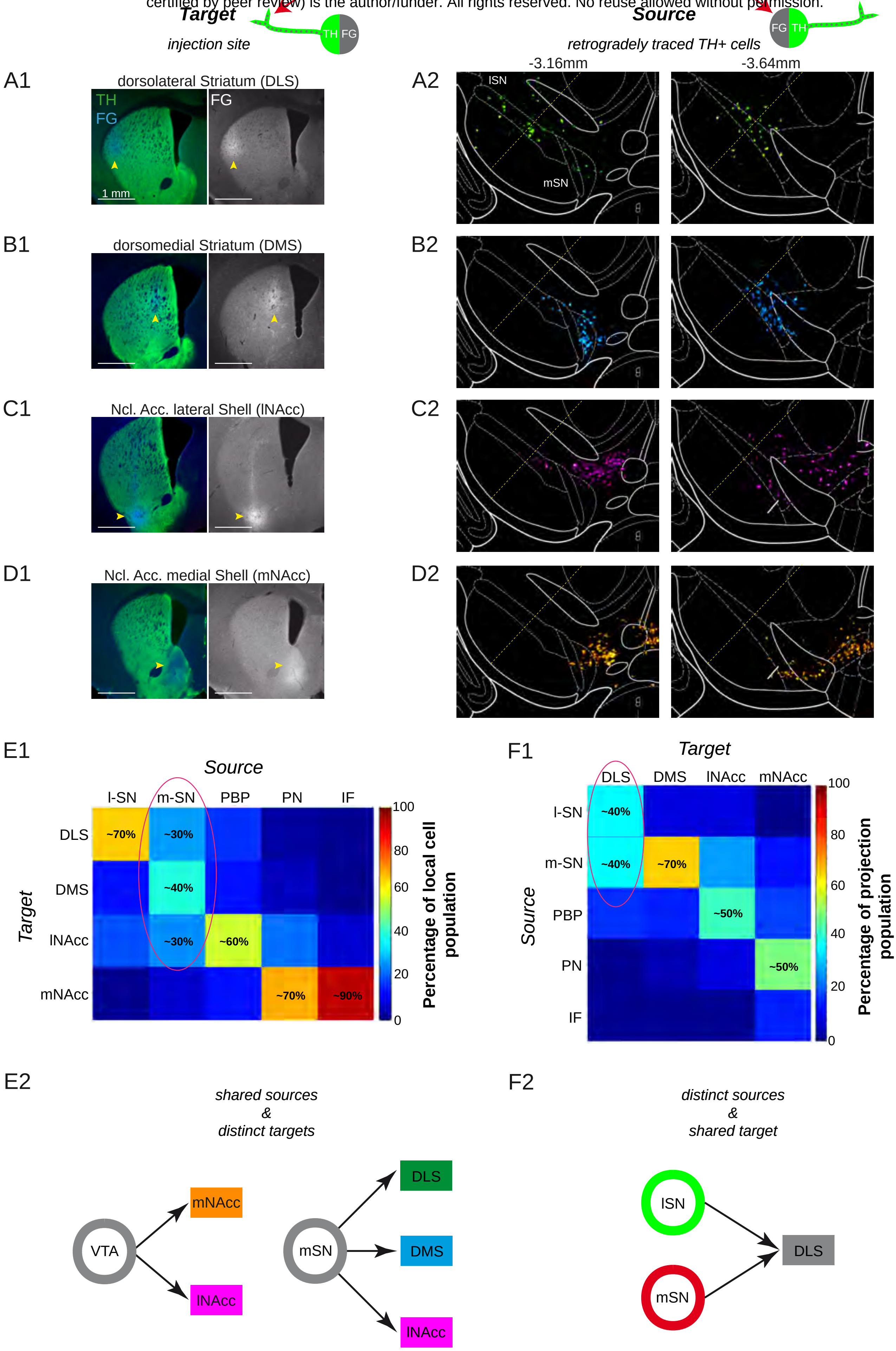

Figure 5

bioRxiv preprint doi: https://doi.org/10.1101/624700; this version posted May 2, 2019. The copyright holder for this preprint (which was not certified by peer review) is the author/funder. All rights reserved. No reuse allowed without permission.

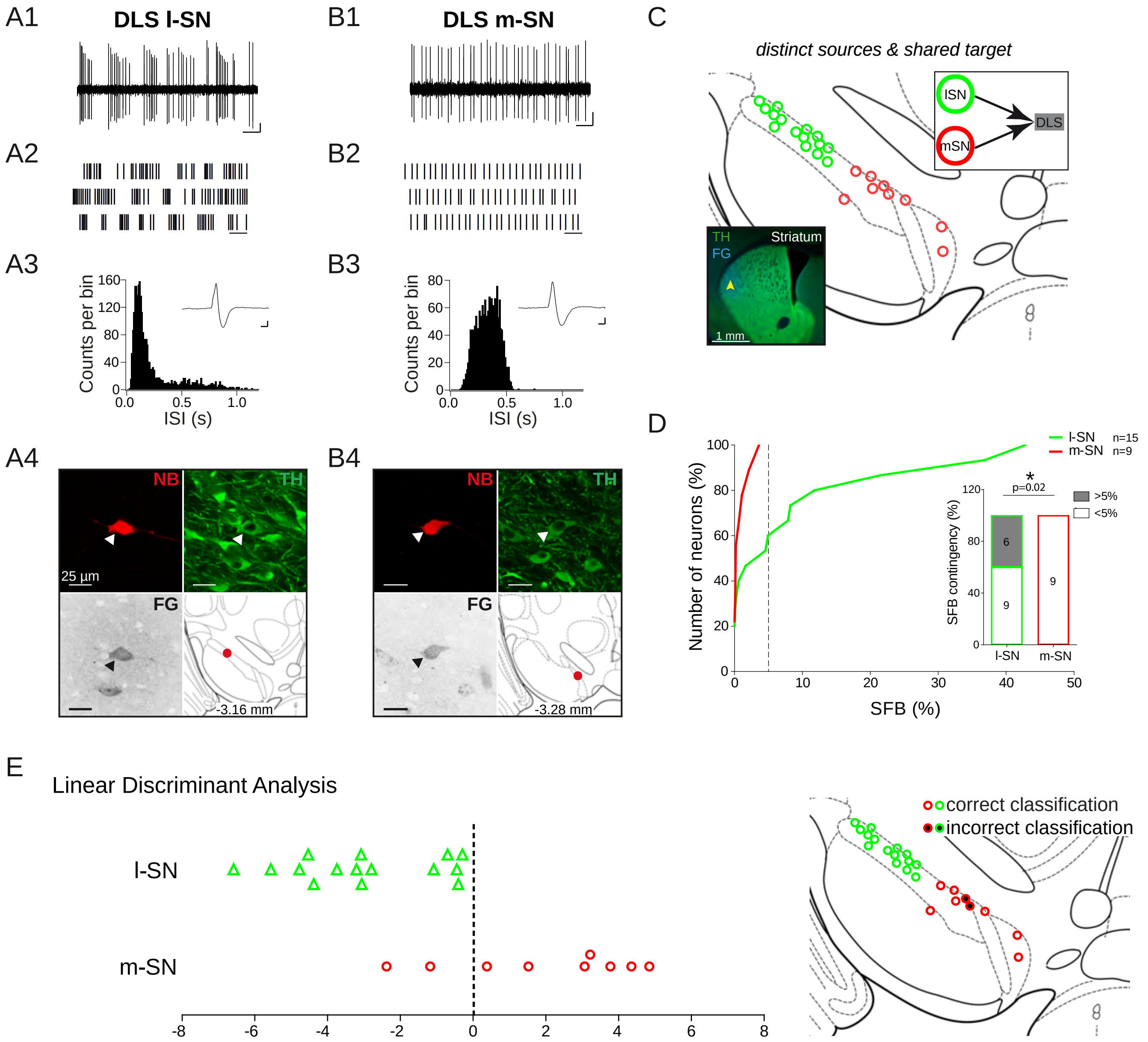

Figure 6

bioRxiv preprint doi: https://doi.org/10.1101/624700; this version posted May 2, 2019. The copyright holder for this preprint (which was not certified by peer review) is the author/funder. All rights reserved. No reuse allowed without permission.

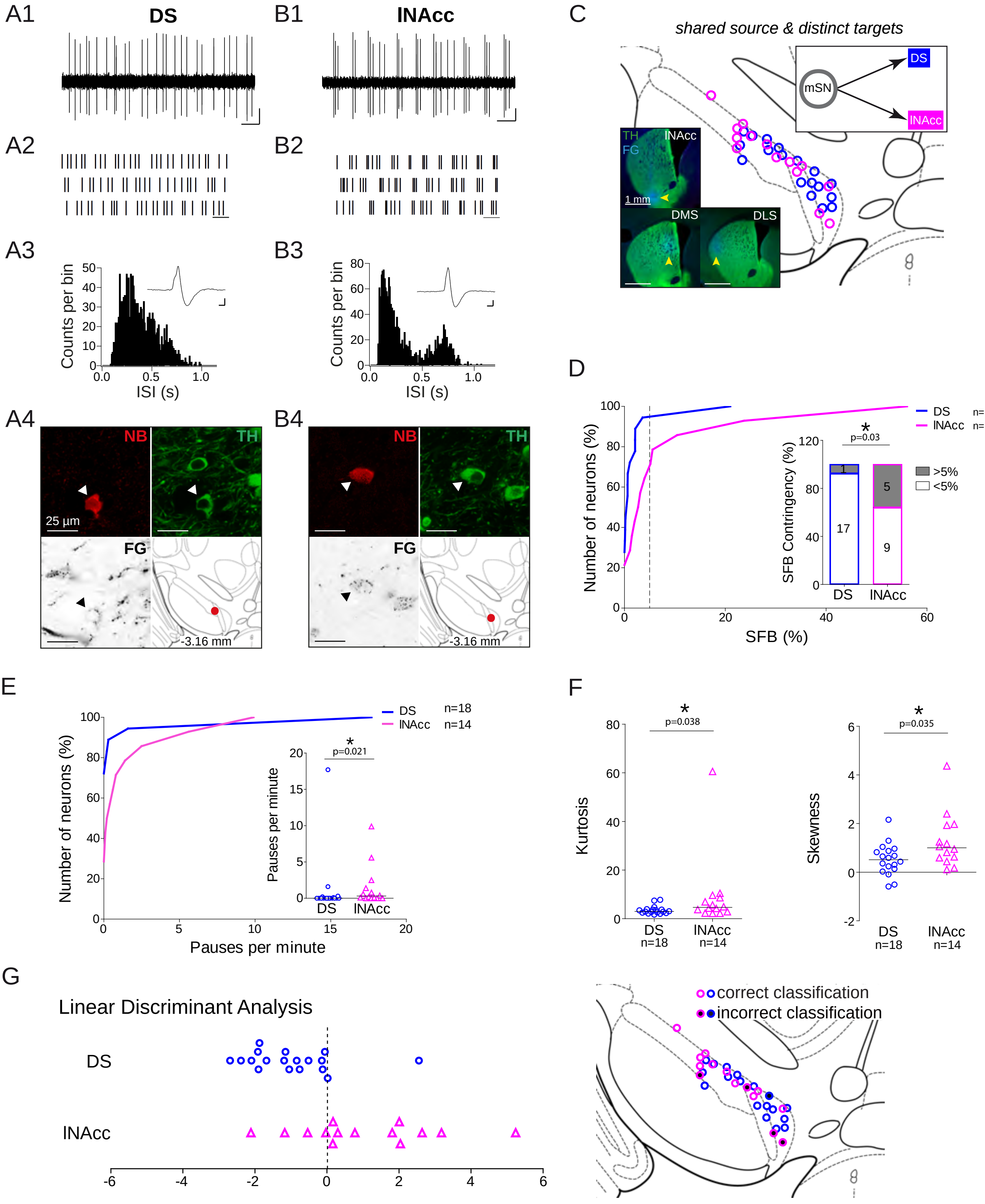

Figure 7

bioRxiv preprint doi: https://doi.org/10.1101/624700; this version posted May 2, 2019. The copyright holder for this preprint (which was not certified by peer review) is the author/funder. All rights reserved. No reuse allowed without permission.

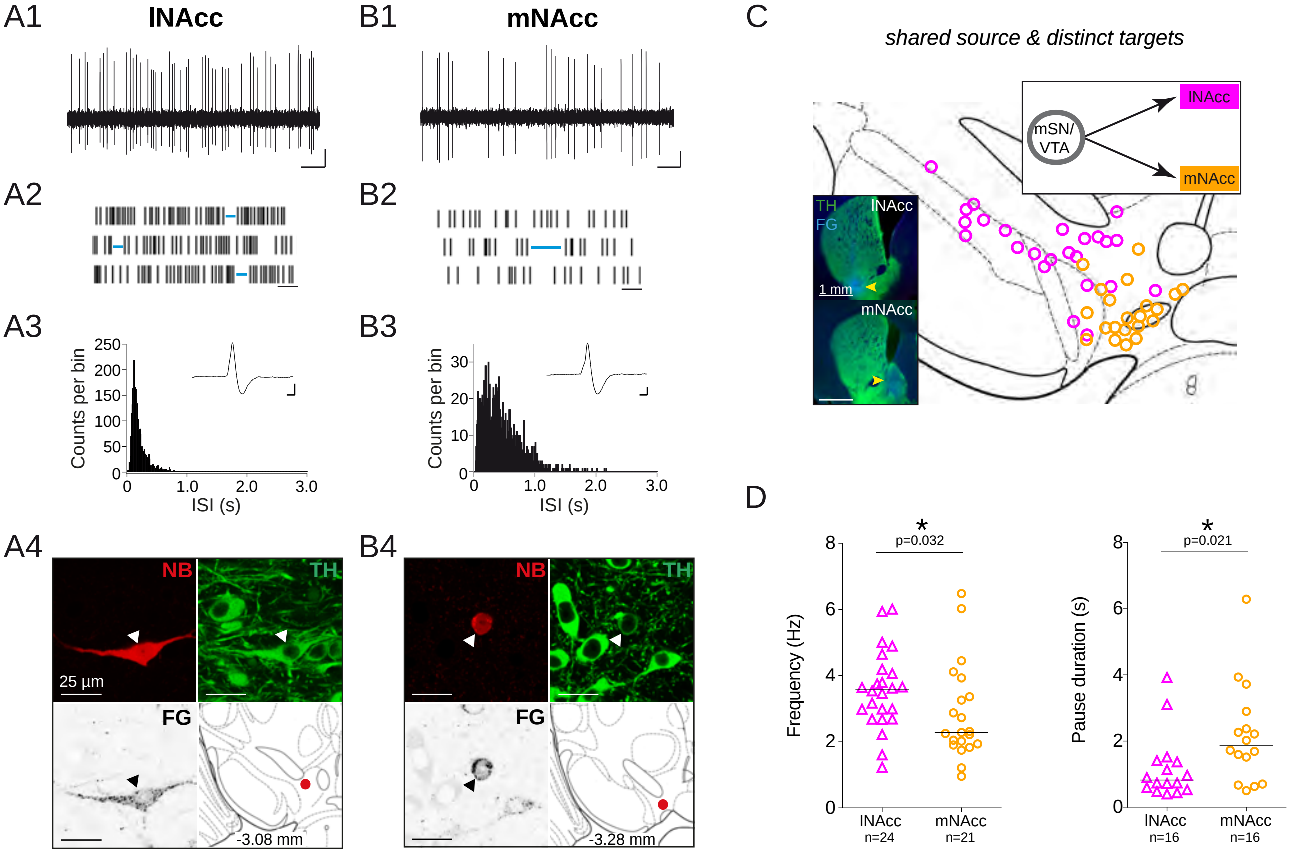

bioRxiv preprint doi: https://doi.org/10.1101/624700; this version posted May 2, 2019. The copyright holder for this preprint (which was not certified by peer review) is the author/funder. All rights reserved. No reuse allowed without permission.

Figure 8